Supplementary material
How Detergent Impacts Membrane Proteins: Atomic-Level Views of Mitochondrial Carriers in Dodecylphosphocholine

Vilius Kurauskas,[†] Audrey Hessel,[†] Peixiang Ma,[†] Paola Lunetti,[‡] Katharina Weinhäupl,[†] Lionel Imbert,[†] Bernhard Brutscher,[†] Martin S. King,[¶] Rémy Sounier,[§] Vincenza Dolce,[‖] Edmund R. S. Kunji,[¶] Loredana Capobianco,[*,‡] Christophe Chipot,[⊥] François Dehez,[*,⊥] Beate Bersch,[†] and Paul Schanda[*,†]

†Univ. Grenoble Alpes, CNRS, CEA, IBS, 38000 Grenoble, France

‡Department of Biological and Environmental Sciences and Technologies, University of Salento, 73100 Lecce, Italy

¶MRC-MBU, Univ. Cambridge, Cambridge CB2 0XY, UK

§CNRS, INSERM, Univ. Montpellier, 34094 Montpellier,France

‖Dept of Pharmacy, Univ. Calabria, 87036 Arcavacata di Rende, Italy

⊥LPCT, UMR 7019 Univ. Lorraine, CNRS and Lab. Internat. Associé Univ. Illinois at Urbana-Champaign, F-54500 Vandoeuvre-lès-Nancy

E-mail: loredana.capobianco@unisalento.it; francois.dehez@univ-lorraine.fr; paul.schanda@ibs.fr

Supplementary Discussion

µs-ms dynamics in the presence of GTP and cardiolipin

We have investigated the effects that addition of GGC1's substrate, GTP, or the functionally important[1,2] lipid cardiolipin (CL) have on dynamics of GGC1. Chemical-shift changes show that GTP and CL as well as POPG interact with GGC1 (see Figure 3 and S20), and we reasoned that at least the presence of substrate would impact GGC1's dynamics. CPMG RD experiments, however show that µs-ms motions are essentially the same as in the absence of GTP. The respective CPMG RD profiles are similar in all investigated cases (apo/with GTP/with CL; Figure S9). Quantitatively, the exchange rate constant in the presence of GTP agrees within error margins with the one in apo state (Figure 2D); the fitted minor-state population is slightly increased by the presence of GTP, but the fitted chemical-shift differences $|\Delta\delta|$ are decreased, such that these changes are likely due to an entanglement of these two fit parameters (see Figure S9B).

The presence of CL slows down the dynamics significantly, by about 2-3 fold. However, the non-functional mutant GGC1$^{2P\rightarrow 2R}$ shows the same behavior as WT protein, suggesting that the presence of CL does not resurrect the protein's functionality (Figure S11 and Table SS1). Put together, the insensitivity of the µs-ms dynamics in DPC to the presence of substrates and function-abolishing mutations suggests that the observed motions are not directly related to function.

Specificity of substrate and inhibitor binding

We have probed the specificity of substrate binding with liposome transport assays. In these experiments we first investigated whether AAC3 can transport GTP. As shown in Table SS3, we find that AAC3 transports specifically ATP but not GTP. This observation, however, might still leave the possibility that AAC3 can at least bind, but not transport GTP. To exclude this possibility, we performed another transport assay, in which a 15-fold excess of GTP over ATP was present, while ATP transport was monitored. If GTP binds to AAC3, it would compete with ATP and thus reduce the transport rate. However, we find that this is not the case (Table SS3), showing that GTP does not bind AAC3. Equivalent experiments with GGC1 demonstrate that ATP does not bind to this protein in lipid bilayers. This observation is in sharp contrast to the behavior found in DPC, where both nucleotides bind to the two proteins in a similar manner, inducing highly similar chemical-shift changes (see main text, Figure 3 and Figure S21).

Previous data have established that ORC1 interacts with, e.g., ornithine and histidine but not with unrelated amino acids such as proline.[3] The high specificity of MCs in lipid bilayers to bind their substrates, reported in many earlier studies and confirmed by our transport assays, provides a solid basis upon which the specificity of binding in DPC micelles can be tested by NMR in a site-specific manner.

Unrestrainted MD simulations of AAC

We performed an initial 700-ns simulation of the bovine AAC (bAAC) in an explicit DPC micelle after removal of the CATR inhibitor. On this timescale the protein conformation does not significantly deviate from the starting structure (Figure S25). However, we observe that the detergent organizes in a non-symmetrical manner around the protein, with an accumulation around H1-H2, compared to H3-H4 and H5-H6. The DPC acyl chains start to protrude between TM helices on the cytoplasmic side (Figure S26). Although this observation might possibly point towards the beginning of a structural distortion, the timescale is too short to draw reliable conclusions.

Simulations of yeast AAC3 in DPC show a similar picture to bovine AAC, i.e., the structure remains close to the crystal structure over several tens of ns. The experimental chemical-shift data have indicated significant structural differences in DPC *vs.* crystal environments (cf. Figures 1D and S4C). Therefore, the conformation observed in this unbiased MD simulation, starting from the crystal structure, does not accurately reflect the secondary structure in DPC. Possibly, the simulation is too short to allow the transition to the conformation that AAC adopts in a DPC. Nonetheless, the observed protrusion of detergent molecules on this time scale might indicate mechanisms of a beginning denaturation.

Materials and methods

Sample preparation

Reagents

1,1',2,2'-tetraoleyl cardiolipin and bovine heart cardiolipin extract were purchased from Avanti Polar Lipids and n-dodecylphosphocholine and 38-^{2}H n-dodecylphosphocholine from Anatrace. Carboxylatractyloside (CATR), guanoside-5'-triphosphate (GTP), adenosine-5'-triphosphate (ATP), $^{15}NH_4Cl$ (98%) and D_2O (98.5%) were obtained from Sigma-Aldrich, $^{13}C_6$-D-glucose (99%) and $^{13}C_6$,1,2,3,4,5,6,6-d_7-D-glucose (98-99%) from Cambridge Isotope Laboratories, Inc, and precursors for labeling of methyl groups in an otherwise deuterated environment from NMR-Bio (Grenoble, France). Gadodiamide, purified from commercially available Omniscan(TM), was a generous gift from Prof. Klaus Zangger (University of Graz, Austria).

Mitochondrial carrier constructs

Figure S1 shows the phylogenetic relationship between the three MCs chosen in this study. Mitochondrial carriers were expressed from codon-optimized, synthetic genes obtained from GeneScript, as follows.

Yeast GGC1 (Uniprot ID:P38988) and GGC1$^{\mathrm{2P}\rightarrow\mathrm{2R}}$ sequences containing C-terminal His$_6$ purification tags were cloned into pET21a(+) vector via NdeI and XhoI sites. In GGC1$^{\mathrm{2P}\rightarrow\mathrm{2R}}$, the two prolines P138 and P230 were mutated to arginines.
The sequence for the wild-type GGC1 expression is the following:

ATGCCGCACACAGATAAGAAGCAGAGTGGGCTGGCGCGCCTGCTGGGTAGTG
CCAGCGCGGGTATTATGGAAATTGCAGTATTTCATCCGGTTGACACTATTAGC
AAACGTCTGATGAGTAACCATACCAAAATTACCTCTGGTCAGGAACTGAATCG

TGTCATCTTTCGCGACCATTTCTCTGAGCCGCTGGGTAAACGTCTGTTTACCCT
GTTTCCGGGTCTGGGCTATGCCGCCTCTTATAAGGTCCTGCAGCGTGTGTATA
AATATGGCGGGCAGCCATTTGCTAATGAATTTCTGAATAAACACTATAAGAAA
GATTTTGATAATCTGTTTGGTGAGAAGACTGGTAAGGCGATGCGTTCTGCTGC
GGCCGGCAGCCTGATCGGTATTGGTGAAATTGTGCTGCTGCCGCTGGACGTGC
TGAAAATCAAACGTCAAACCAACCCGGAATCTTTTAAAGGTCGTGGCTTCATT
AAAATCCTGCGCGATGAAGGCCTGTTTAACCTGTACCGCGGCTGGGGTTGGAC
GGCGGCTCGTAATGCGCCGGGCTCTTTTGCGCTGTTCGGTGGCAACGCTTTTG
CAAAGGAGTACATTCTGGGGCTGAAAGATTACTCTCAGGCCACATGGAGCCAG
AATTTTATCAGCAGCATTGTGGGCGCGTGCTCTAGTCTGATCGTAAGTGCACC
ACTGGATGTTATTAAAACGCGCATCCAAAATCGCAATTTCGACAACCCAGAGA
GTGGCCTGCGCATCGTCAAGAACACCCTGAAGAACGAGGGCGTTACTGCATTC
TTCAAAGGCCTGACCCCTAAACTGCTGACGACGGGCCCTAAACTGGTTTTCAG
CTTCGCCCTGGCACAAAGCCTGATTCCTCGCTTCGATAACCTGCTGAGCAAGCT
CGAGCACCACCACCACCACCACTGA

Yeast ORC1 (Uniprot ID:Q12375) construct containing N-terminal His_8 tag was cloned into pET28a vector via NcoI and XhoI sites. The nucleotide sequence used for ORC1 expression is the following:

ATGGATCATCATCATCATCATCATCATCATGAAGATAGCAAGAAGAAAGGATT
GATCGAGGGCGCAATTCTGGATATTATTAATGGCTCGATCGCCGGTGCCTGTG
GCAAAGTGATTGAATTCCCGTTTGATACCGTGAAGGTTCGTCTGCAAACGCAG
GCCTCCAACGTATTCCCCACAACCTGGTCATGCATCAAGTTCACCTATCAGAAC
GAAGGCATTGCCCGGGGATTTTTCCAGGGTATTGCGTCACCGCTGGTCGGCGC
GTGCCTGGAAAACGCGACGCTGTTTGTCAGCTATAACCAGTGTAGTAAATTCC
TGGAAAAACATACCAATGTTTCTCCTTTAGGTCAGATTCTCATCAGCGGCGGC

GTTGCTGGTAGCTGTGCGTCGTTAGTACTGACGCCAGTGGAGCTTGTGAAATG
CAAACTGCAAGTCGCAAATTTGCAGGTGGCTTCGGCGAAAACCAAACATACTA
AGGTGCTGCCAACAATCAAAGCGATTATCACCGAGCGCGGCTTAGCAGGTTTA
TGGCAAGGGCAAAGTGGGACGTTTATCCGAGAAAGTTTTGGCGGTGTTGCCTG
GTTTGCCACCTACGAAATTGTCAAAAAATCGTTGAAAGACCGTCACAGCCTGG
ACGATCCGAAACGCGATGAAAGCAAAATCTGGGAACTACTGATATCCGGAGGC
TCTGCAGGGCTGGCGTTTAACGCCAGCATTTTTCCGGCAGACACCGTTAAATC
CGTGATGCAGACTGAGCACATTTCTCTTACCAACGCAGTAAAAAGATTTTCG
GTAAATTTGGTTTGAAAGGCTTTTACCGTGGTCTGGGGATCACTCTGTTCCGC
GCTGTGCCGGCGAATGCCGCTGTTTTCTATATCTTTGAAACGCTTTCAGCGCT
GTAA

Yeast AAC3$^{\ominus\text{c-saltbridge}}$ mutant was expressed in pET21a(+) vector. The sequence used was nearly identical to the one reported by[4] for wild-type AAC3 (Uniprot ID:P18238) (containing N-terminal His$_{10}$ purification tag in the long, 26 residue N-terminal extension). AAC3 from[4] and yAAC3$^{\ominus\text{c-saltbridge}}$ mutant differ by the following substitutions in the putative cytosolic salt-bridge network: K101D, K204D, Q298D. Furthermore, in this study as well as the one by Brüschweiler *et al*,[4] the four Cys residues of WT AAC3 were mutated, in order to increase stability. In the work of Brüschweiler *et al* these mutations were: C62A, C260A, C233V and C277A, while in the present study they were C62A, C260A, C233A and C277S. The resulting nucleotide sequence is the following:

ATGGCAAGCATGACTGGTGGTCAGCAGATGGGTCGTGGTTCTCACCACCATCA
CCACCACCACCATCATCACCTGGTACCGATGTCTTCTGATGCTAAGCAGCAGG
AAACTAACTTCGCTATCAACTTCCTGATGGGTGGTGTGAGCGCAGCAATCGCA
AAGACTGCTGCTTCTCCGATTGAACGTGTGAAGATCCTGATCCAGAACCAGGA
CGAAATGATCAAGCAGGGCACCCTGGACAAGAAGTACAGCGGTATCGTGGACG

CTTTCAAACGCACTGCAAAACAGGAGGGTCTGATCTCCTTCTGGCGTGGTAAC
ACTGCAAACGTGATCCGTTACTTCCCGACCCAGGCACTGAACTTCGCATTCAAA
GACAAAATCAAACTGATGTTCGGCTTCAAAAAAGAGGAAGGCTACGGCAAATG
GTTCGCGGGTAACCTGGCGAGCGGTGGTGCGGCTGGTGCACTGTCTCTGCTGT
TCGTGTACTCCCTGGACTTCGCACGTACTCGTCTGGCTGCTGATGCTAAAAGC
TCTAAAAAAGGCGGTGCTCGTCAGTTCAACGGTCTGACCGACGTTTACAAAAA
AACCCTGAAATCCGACGGTATCGCGGGCCTGTACCGTGGTTTCATGCCGTCTG
TGGTAGGTATCGTAGTTTACCGCGGTCTGTATTTCGGCATGTTTGACTCCCTG
AAACCGCTGGTACTGACCGGTTCCCTGGATGGTTCTTTTCTGGCGTCTTTTCT
GCTGGGCTGGGTAGTTACCACCGGCGCTTCTACCGCGAGCTATCCGCTGGATA
CCGTTCGTCGCCGCATGATGATGACCAGCGGCCAGGCGGTTAAATATAACGGC
GCGATTGATGCGCTGAAAAAAATTGTTGCGTCCGAAGGCGTTGGCTCCCTGTT
TAAAGGCAGCGGCGCGAACATTCTGCGCTCCGTTGCGGGCGCGGGCGTTATTT
CCATGTATGATCAGCTGCAGATGATTCTGTTTGGCAAAAAATTTAAATAA

Production of AAC3 in yeast and thermostability shift assay experiments

Construction of yeast AAC3 expression strains

The codon-optimised ScAAC3 gene was synthesised with an N-terminal eight-histidine tag and Factor Xa cleavage site (Genscript) and cloned into the yeast expression vector pYES-PMIR2-AAC2.[5] Expression vectors were transformed by electroporation into *Saccharomyces cerevisiae* strain WB12 (MATαade2-1 trp1-1 ura3-1 can1-100 aac1::LEU2 aac2::HIS3),[6] which lacks functional Aac1p and Aac2p carriers. Transformants were selected initially on SC medium minus tryptophan plates, and then on YPG plates, confirming the expression of functional ADP/ATP carriers.

Preparation of lipid

Tetraoleoyl cardiolipin, dissolved in chloroform, was purchased from Avanti Polar Lipids (Alabaster, Alabama). Typically, 100 mg of lipid was dispensed into a glass vial, and chloroform was removed by evaporation under a stream of nitrogen. Lipids were solubilized in 10% (w/v) dodecylmaltoside by vortexing for 4 hours at room temperature to give a 10 mg.ml^{-1} lipid in 10% detergent stock. The stocks were snap-frozen and stored in liquid nitrogen.

Purification of ScAAC3 for thermostability analysis

A five-liter pre-culture was used to inoculate 50 liter of YPG medium in an Applikon 140 Pilot System with an eZ controller. Cells were grown at 30 C for 72 hours, and harvested by centrifugation (4,000 g, 20 minutes, 4 C). Mitochondria were prepared with established methods,[7] flash frozen in liquid nitrogen, and stored at -80 C until use. Protein was purified, as previously described.[8] In brief, isolated yeast mitochondria (1 g total protein) were solubilized in 2% dodecylmaltoside (Glycon), particulate material removed by ultracentrifugation, and the soluble fraction loaded onto a Ni-Sepharose high performance column. The column was washed with buffer containing 0.1 % dodecylmaltoside and 0.1 mg ml-1 tetraoleoyl cardiolipin (18:1), resuspended with buffer and incubated at 10 C overnight in the presence of Factor Xa. The cleaved protein was separated from the nickel sepharose media by filtration, the concentration determined by BCA, and the protein snap-frozen and stored in liquid nitrogen.

Thermostability analysis

Thermostability data were obtained by using the thiol-reactive fluorophore N-[4-(7-diethylamino-4-methyl-3-coumarinyl)phenyl] maleimide (CPM), which undergoes an increase in fluorescence emission following reaction with cysteine residues.[9] A rapid procedure using a rotary qPCR machine was used, as described previously.[10] For this purpose, a 5 mg.ml^{-1} stock of CPM dissolved in DMSO was diluted 50-fold into buffer containing 20 mM HEPES pH 8.0, 100 mM NaCl, 0.1% dodecylmaltoside and 0.1 mg.ml^{-1} tetraoleoyl cardiolipin, vortexed and the solution was allowed to equilibrate in the dark at room temperature for 10 min. To exchange detergent, approximately 2 µg of protein was added into a final volume of 45 µL buffer B containing either 0.1% dodecylmaltoside with 0.1 mg ml -1 tetraoleoyl cardiolipin, 0.1% dodecyl phosphocholine with 0.1 mg ml^{-1} tetraoleoyl cardiolipin or 0.1% lauryl maltose neopentyl glycol with 0.1 mg.mg^{-1} tetraoleoyl cardiolipin. CPM working solution was added (5 µL), and the solution was vortexed and allowed to equilibrate in the dark for 10 min at room temperature in the presence of 10 µM carboxyatractyloside, or on ice in the dark without inhibitor. Fluorescence of the CPM dye was measured on a Qiagen Rotorgene Q using the HRM channel, which provides excitation light at 440-480 nm with emission detected at 505-515 nm. Measurements were made in 1 C intervals from 25 – 90 C with a 'wait between reading' set to 4 sec, which equated to a ramp rate of 5.6 C/min, following an initial pre-incubation step of 90 seconds. Data were analyzed and melting temperatures (the inflexion point of the melting curve) were determined with the software supplied with the instrument.

Protein expression in *E. coli* for NMR studies

All samples studied by NMR were expressed in M9 medium[1] containing $^{15}NH_4Cl$ and $^{13}C_6$-D-glucose (or $^{13}C_6$,1,2,3,4,5,6,6-d_7-D-glucose) as the only sources of nitrogen and carbon, respectively. Furthermore, as the system we studied is large for solution state NMR standards ≈50-60 kDa, the protein was highly enriched with ^2H. This enrichment was achieved by growing the BL21(DE3) *E. coli* strains in ≈98% D_2O. D_2O is generally toxic to bacteria, therefore adaptation was required, by first inoculating the bacteria in Lysogeny Broth[2], then in subsequent steps the culture was grown in H_2O M9 medium, 1:1 H_2O:D_2O medium and the final preculture was obtained by growing bacteria in 98% D_2O. This preculture was used

---

[1] 37.3 mM Na_2HPO_4, 22 mM KH_2PO_4, 8.56 mM NaCl, 18.4 mM $^{15}NH_4Cl$, 0.2% glucose, 1 mM $MgCl_2$, 100 µM $CaCl_2$, 100 µM $MnCl_2$, 50 µM $ZnCl_2$, 50 µM $FeCl_3$, vitamin supplements and either 100mg/l of ampicilin or 30mg/l of kanamycin

[2] 10 g/l tryptone, 5 g/l yeast extract, 5 g/l NaCl

to inoculate 0.5 l of D_2O-M9 medium. The temperature in all the steps was 37° C, and the shaking speed and flask sizes were chosen to allow adequate aeration (generally 1:10 for precultures and 1:4-1:6 culture:flask volume for the final cultures). After BL21(DE3) *E. coli* containing the expression vectors with mitochondrial carrier genes reached exponential growth phase (OD_{600} ≈0.6), the protein expression was induced by addition of 1 mM IPTG. For GGC1 and AAC3 the proteins were expressed for 3-4 hours at 37° C and for ORC1 at 20° C overnight.

The sample of GGC1 with specific methyl labeling ([U-^{2}H], A-[$^{13}CH_3$]β, L-[$^{13}CH_3$]proS, V-[$^{13}CH_3$]proS-labelled) was prepared in fully deuterated medium (as above), with the addition of the following precursors one hour before induction: 700 mg/L of ^{2}H-$^{13}CH_3$-Alanine (^{13}C 99%; ^{2}H 98%), 300 mg/L of ^{2}H-$^{13}CH_3$-2-hydroxy-2-methyl-3-oxo-4-butanoic acid (^{13}C 99%; ^{2}H 95%) and 60 mg/L of ^{2}H-L-Isoleucine (^{2}H 98%).

We have also used an approach to facilitate the assignment of ORC1, termed reverse labeling, which consists of adding one or more amino acids in unlabeled form. In these cultures, M9 medium for uniform ^{13}C,^{15}N labeling was supplemented 30 minutes prior to induction by 100 mg/L of unlabeled V, R, K, T, L, I or F.

Protein purification (*S. cerevisiae* ORC1)

Bacterial pellets from 350-500 ml of cell culture were resuspended in 40 ml sonication buffer[3]. The sample was divided into two parts and each part was sonicated separately to increase the efficiency (Sonics VC505 ultrasonic processor with 13 mm probe) by applying 2 second pulses with 2-10 second breaks at 30% of power for 10-15 minutes of total pulse duration. The sonicated bacteria were centrifuged (40000 g, 15 minutes at 4° C), and the pellets containing inclusion bodies were resuspended in 3 ml of 3% sarkosyl, 1 mM TCEP, 1 mM EDTA and incubated for 2-3 hours at room temperature in the presence of lysozyme and DNAse.

---

[3] 50 mM TrisCl pH 7.0, 1 mM PMSF, 5% glycerol, 1 µg/ml leupeptin, 1 µg/ml pepstatin, 1 mM TCEP and 1mM EDTA

After the incubation in sarkosyl the sample was centrifuged again to remove the insoluble debris (40000g, 30 minutes, 4° C). The sample (≈3-3.5 ml) was refolded by flash-dilution, slowly adding drops of sarkosyl-dissolved ORC1 to 35-40 ml of 50 mM NaH_2PO_4:Na_2HPO_4 (pH 7.5), 100 mM NaCl and 1.5 mM DPC, 1 mM TCEP, 0.02 mg/ml 1,1',2,2'-tetraoleylcardiolipin buffer at 4° C. Refolded ORC1 containing His_8 purification tag was bound to 12 ml of NiNTA resin, previously equilibrated with the refolding buffer and incubated overnight at 4° C by gentle mixing. Afterwards, the resin was washed on a gravity flow column with 10 resin volumes of refolding buffer supplemented with 30 mM of imidazol, where the DPC concentration was increased to 3 mM and TCEP concentration reduced to 0.5 mM in order to avoid the reduction of Ni^{2+} ions. The samples were eluted by incrementing imidazol concentration in two steps by applying 1 column volume of refolding buffer containing 200 or 500 mM of imidazol, 15 mM DPC and 0.5 mM TCEP at each step. After this step of purification, the ORC1 sample was concentrated to no more than 3-3.5 mg/ml and subjected to gel filtration on HiLoad Superdex 200 16/60 prep grade column using 50 mM MES pH 6.5, 100 mM NaCl, 1 mM EDTA, 1 mM TCEP, 1 mM PMSF, 1 µg/ml leupeptin, 1 µg/ml pepstatin, 3 mM DPC buffer. Gel filtration profiles showed that the sample was homogeneous. The collected fractions were analysed by SDS-PAGE and the purest fractions were pooled to obtain the final sample. The sample was afterwards concentrated and desalted on a concentrating tube by using the gel-filtration buffer with no NaCl. The protein yield was around 15 mg of ORC1 per liter of cell culture. Final concentrations of ORC1 used for NMR were in a range of 500 to 1000 µM.

We have further investigated the oligomerisation state of obtained ORC1 under conditions close to those used in NMR samples (concentration of the protein ≈150 µM). A single peak was observed on AUC profiles, with a sedimentation coefficient in agreement with a monomeric state (Figure S2).

Protein purification (*S. cerevisiae* GGC1)

For GGC1 purification we have used the protocol from reference.[11] Briefly, bacterial pellets from 500 ml of cell culture were resuspended in 20 mM HEPES pH 7.5, 150 mM NaCl, 0.1 mM PMSF, 10 mM β-mercaptoethanol buffer and sonicated as described above for ORC1. The pellets were collected by centrifugation at 40000g for 15-30 minutes at 4° C. The resulting inclusion bodies were dissolved in a buffer containing 20 mM HEPES pH 7.5, 150 NaCl, 3M guanidinium hydrochloride, 1% Triton X-100 and 5 mM β-mercaptoethanol overnight at 4° C upon gentle stirring. The insoluble debris were removed by centrifugation at 40000g for 15-30 minutes at 4° C and the supernatant applied to 12 mL NiNTA resin in the presence of 10 mM imidazole on a gravity-flow column. The flow-through was reapplied on the column again to increase the fraction of bound GGC1. The columns containing bound protein were washed with three column volumes of each buffer in the following order: 1) 20 mM HEPES pH 7.5, 150 NaCl, 3M guanidinium hydrochloride, 1% Triton X-100, 5 mM β-mercaptoethanol; 2) 20 mM HEPES pH 7.5, 150 NaCl, 0.1% Triton X-100, 5 mM β-mercaptoethanol; 3) 20 mM HEPES pH 7.5, 150 NaCl, 3 mM DPC, 5 mM β-mercaptoethanol. The protein was eluted with 3 column volumes of the buffer used in the step 3 of washing, but supplemented with 250 mM of imidazol. Afterwards, the protein was concentrated to ≈5 mg/ml with an ultrafiltration device (Amicon) and applied on a HiLoad Superdex 200 16/60 prep grade gel filtration column, using 50 MES pH 6, 150 NaCl, 3 mM DPC and 2 mM β-mercaptoethanol buffer. The resulting fractions were analyzed by SDS-PAGE and selected based on purity for preparation of the NMR sample. The protein was concentrated and desalted, as ORC1. The yield of GGC1 is even higher, amounting to 30-40 mg per liter of cell culture.

GGC1$^{\mathrm{2P\rightarrow 2R}}$ was purified the same way as wild-type GGC1, and the behaviour was nearly identical (the yield was actually slightly higher).

$\mathrm{CH_3}$-ALV-[^{15}N, ^{13}C, D] GGC1 was purified the same way as wild-type GGC1. After the gel-filtration, the sample was applied to NiNTA column and washed with 5 column volumes of a 50 mM MES pH 6, 100 mM NaCl, 3 mM ^{2}H-DPC. The sample was eluted with the same buffer supplemented with 200 mM imidazol. Imidazol was removed by multiple steps of concentration and subsequent dilution with a buffer containing no imidazol.

Investigations of GGC1 samples by AUC also indicated that the protein is monomeric at 150 µM concentrations (Figure S2). However, the sedimentation coefficient appeared to be larger for GGC1 as compared to ORC1, despite the two proteins having very similar molecular weight. This observation might indicated that the hydrophobic regions of the proteins are solvated differently in the presence of DPC micelles.

Protein purification (*S. cerevisiae* AAC3$^{\ominus\text{c-saltbridge}}$ mutant)

AAC3$^{\ominus\text{c-saltbridge}}$ mutant was purified as reported previously,[4] with several modifications to the protocol. Briefly, the cell pellets were sonicated in a 20 mM HEPES pH 7.4, 150 mM NaCl, 30 mM lysozyme and 1mM β-mercaptoethanol buffer. The inclusion bodies were collected by centrifugation at 20000 g for 30 minutes. The inclusion bodies were solubilized in 4ml of 20 mM HEPES, 150 mM NaCl, 1.5% sarkosyl, 0.05% polyethylene glycol 4000 and 1 mM β-mercaptoethanol buffer overnight at 4° C. The insoluble debris were removed by centrifugation at 40000 g for 30 minutes. Supernatant containing solubilized AAC3$^{\ominus\text{c-saltbridge}}$ mutant was refolded by flash-dilution into a buffer containing 20 mM HEPES pH 7.4, 150 mM NaCl, 20 mM imidazol and 6 mM DPC, resulting in 10-fold overall dilution. Refolded AAC3$^{\ominus\text{c-saltbridge}}$ mutant was applied on NiNTA resin (2 ml for 1 l of cell culture). The protein was eluted with a buffer containing 20 mM HEPES pH 7.4, 150 mM NaCl and 200 mM imidazol. AAC3$^{\ominus\text{c-saltbridge}}$ mutant was then dialyzed for 4 hours in 20 mM HEPES pH 7.4, 30 mM NaCl, 3 mM DPC buffer and applied on a Hi-trap Q FF column. The non-bound fraction was applied on an analytical gel-filtration column (Superdex 10/300 GL) in the presence of 30 mM MES pH 6, 20 mM NaCl, 5 mM β-mercaptoethanol, 3 mM DPC buffer. The gel-filtration profile contained at least three overlapping peaks. The peak corresponding to the monomer of AAC3$^{\ominus\text{c-saltbridge}}$ mutant was re-injected on the gel-filtration column and the resulting profile contained a single peak with a small shoulder, providing sufficient purity for NMR experiments. The typical yield was 2 mg from one liter of D_2O M9 culture.

Titration of mitochondrial carrier samples with different molecules

Solutes (GTP, ATP, l-ornithine, l-proline, l-histidine, NaCl, CATR, gadodiamide) used for the titration experiments were dissolved in the flow-through buffer obtained after the last step of sample concentration. The pH was carefully measured after addition of ≈10 times more of the intended solute to the buffer which did not contain protein, and if necessary was adjusted by NaOH (in all the cases the added solute only acidified the buffer), so that the pH of the sample containing protein would not be affected. The solute dissolved in the flow-through buffer was then added to the protein containing sample using accurate eVol (SGE Analytical Science) pipettes to reach the required concentration.

Cardiolipin and POPG stock solutions were in chloroform. To titrate these lipids, the chloroform was first evaporated under the nitrogen flow and the lipids were dissolved in ultrapure water ($R=18.2\ M\Omega\cdot cm$) at known concentration. The NMR sample volume was carefully measured to estimate the required amount of lipid to achieve intended concentration, and an aliquote containing required amount of lipid was freeze-dried overnight. The lipid was then dissolved in the NMR sample. We have measured if it affected the pH beforehand, dissolving an extra aliquote of lipid in a buffer containing no protein.

Transport activity measurements in liposomes

AAC3, GGC1 and mutants thereof were expressed in *E. coli* BL21(DE3) as inclusion bodies (IB) and purified as previously described.[12] The purified IB were suspended in a buffer consisting of 10 mM Tris-HCl pH 7.4 and solubilized in 1.67% sarkosyl for 20 minutes at 0°C. The solution obtained was diluted twenty times with buffer containing 10 mM PIPES, pH 7.0 and centrifuged at 12.000 rpm for 10 minutes at 4 °C. For actitivity measurements the supernatant (extract) was reconstituted into liposomes as previously described.[13] In addition to this well-established protocol, we also tried a similar protocol that involves dodecylphosphocholine (DPC). The aim of these experiments was to probe whether DPC irreversibly inactivates MCs, or whether their activity could be resurrected after reconstitution and removal of detergent. In this protocol, IB were solubilized with buffer containing 1.67% (w/v) sarkosyl and 10 mM PIPES, pH 7.0. After solubilization at 4 °C for 20 min, the solution was diluted twenty times with a buffer containing 6 mM DPC, 10 mM PIPES, pH 7.0 and centrifuged at 12.000 rpm for 10 minutes at 4°C.

For actitivity measurements, the purified recombinant proteins were reconstituted into an artificial membrane system. Liposomes were obtained by sonicating (Branson 250, Branson Ultrasonics Corporation) egg yolk phospholipids, at a concentration of 100 mg/ml, for 10 minutes at 40 watts at 2C, with 1 second pulse followed by 2 seconds pause. Subsequently, a reconstitution mixture was prepared, consisting of purified protein (100 µl with 0.5-1 µg of protein), 1.3% Triton X-114, 1.4% phospholipids (as liposomes), 20 mM PIPES, pH 7.0, 5 mM substrate (GDP in the case of GGC1 or ATP in the case of AAC3), and 1.14 mg/ml CL (about 3% of phospholipids) at pH 7.0. These components were mixed thoroughly, and passed through an Amberlite column (Bio-Rad) which was pre-equilibrated with 20 mM PIPES at pH 7.0. All operations were performed at 4°C, except for the passages through Amberlite, which were carried out at room temperature. External substrate was removed from proteoliposomes on Sephadex G-75 columns, pre-equilibrated with 20 mM NaCl and 10 mM PIPES at pH 7.0. The same buffer is used for elution. The first 600 µl of slightly turbid eluate, containing the proteoliposomes, are collected. Transport at 25°C was started by adding, at the indicated concentrations, ^{3}H-[GTP] or ^{3}H-[ATP] (Scopus Research BV, The Netherlands) to substrate-loaded proteoliposomes (exchange). In both cases, transport was terminated by adding of 30 mM PLP and 10 mM BAT, which in combination and at high concentrations completely inhibit the activity of several mitochondrial carriers. In control samples, the inhibitors were added at time 0 together with the radioactive substrate according to the "inhibitor stop method".[13]

The amount of reconstituted protein was assayed by densitometric analysis (Model GS-700 Imaging Densitometer, Bio-Rad) on denaturing polyacrylamide gel, using carbonic anhydrase as protein standard.[14] To check if the protein was inserted into the liposomes (and not just aggregated on the surface) proteoliposomes were treated with an alkaline solution. Both the soluble and proteoliposome fractions were analysed by SDS-PAGE. Aggregated protein would be expected to be removed from the liposomes by neutralizing the charge of the lipids. No protein was solublized with this alkaline treatment, demonstrating that the proteins were inserted.

NMR experiments and analysis

Acquisition and processing of NMR spectra

All NMR data were acquired on 600, 700, 850 or 950 MHz Bruker spectrometers equipped with cryogenic probes and controlled by Topspin 3.2 software. Unless stated otherwise, NMR experiments were recorded at a sample temperature of 30°C. The spectra were processed using nmrPipe software. For 4D experiments (assignment experiments of ORC1 with HNCACO and HNCOCA) non-uniform acquisition was applied (as for the 4D spectra), and the MDD software[15] together with NMRPipe[16] was used for processing.

Chemical shift perturbation analysis

The assignment of spectra after titration with a particular molecule was obtained after manually comparing the spectra with the spectra of apo protein using CcpNmr software.[17] In case of larger chemical shift perturbations, as for cardiolipin, the spectra were recorded at multiple concentrations of the molecule. For GGC1$^{\mathrm{2P\rightarrow 2R}}$ assignment we have recorded additional HNCO, HN(CA)CO, HNCACB and ^{15}N,(^{1}H)-HSQC-NOESY-^{15}N,^{1}H-HSQC spectra. The magnitudes of chemical shift perturbations were calculated using in-house scripts, with the equation:

$$\Delta\delta = \sqrt{(\delta_H^i)^2 + (-4.316/42.576)^2 \cdot (\delta_N^i)^2 + (10.705/42.576)^2 \cdot (\delta_C^{i-1})^2} \tag{1}$$

δ_X in the equation corresponds to the chemical shift perturbation on a single dimension. The constants are the gyromagnetic ratios of γ_N or γ_C and γ_H.

ORC1 assignment

For ORC1 assignment we have recorded BEST-TROSY versions of HNCA, HN(CO)CA, HN(CA)CB, HN(CO)CACB, HN(CA)CO and HNCO as well as ^{15}N,(^{1}H)-HSQC-NOESY-^{15}N,^{1}H-HSQC experiments and 4D HNCACO and HNCOCA spectra. In addition, reverse-labeled samples were prepared where all amino acids were isotopically enriched with ^{15}N and ^{13}C, except either Ile, Leu, Phe, Thr, Val, Lys or Arg, which were added in unlabeled form (i.e., seven separate samples). 3D HNCO experiments were recorded with these reverse-labeled samples, and the signals of the respective amino acid types were missing, thus facilitating assignment. The partial residue-specific assignment of ORC1 is reported in table S5.

Assignment of methyl groups of GGC1

Backbone assignment of GGC1 had been reported earlier.[18]

Methyl assignment of Ala, Leu and Val sample was obtained using a set of 2D ^{15}N-HSQC, 2D ^{13}C-SOFAST, 3D ^{13}C-HSQC-NOESY-^{15}N-HSQC and ^{15}N-HSQC- NOESY-^{13}C-HSQC experiments. The mixing time for NOESY experiments was 278 ms. To avoid the interference of aliphatic proton signals from DPC, we have used deuterated DPC with all ^{1}H atoms exchanged to ^{2}H for all methyl experiments used in this study (assignment and CPMG experiments).

CPMG data collection

All CPMG data were collected at 30° C. Backbone ^{15} N CPMG data were recorded either as a 3D TROSY-HNCO type experiments (for the majority of data sets) or 2D TROSY-HN data sets. Table S1 states which data sets were collected as 2D (HN-based) or 3D (HNCO-based) experiments.

The pulse sequence for the 3D HNCO version was used similar to ref.,[4] except that we have used shaped pulses to avoid excitation of aliphatic protons and thus gain sensitivity.[19] The 2D version was used as reported previously.[20] Methyl CPMG relaxation dispersion data were collected with a MQ version.[21] Reference spectra (I_0) for the calculation of $R_{2,\mathrm{eff}}$ (see section below) were recorded in the absence of a CPMG delay. 20 ms CPMG delays were used to record following CPMG data: 600, 700, 850 MHz GGC1-CH_3, 600, 950 MHz AAC3$^{\ominus\text{c-saltbridge}}$ mutant, 600, 850 MHz GGC1$^{2P\rightarrow 2R}$ with cardiolipin, 700, 850 MHz GGC1 with cardiolipin, 700 MHz GGC1 with cardiolipin and GTP.

40 ms relaxation delay was used for: 600, 850 MHz GGC1 with GTP, 750, 850 MHz apo GGC1, 600, 850 MHz apo GGC1$^{2P\rightarrow 2R}$, 600 MHz GGC1 with cardiolipin, 600 MHz GGC1 with cardiolipin and GTP, 600, 700 MHz ORC1. We could not observe the difference in the relaxation curves due to a different delay length, and therefore utilized shorter delays in the later experiments to reduce the effect of transverse relaxation and increase sensitivity (at the expense of giving up the lowest achievable CPMG frequencies).

CPMG data analysis

CPMG spectra were processed using NMRPipe.[16] The peak volumes were quantified using nmrView Java software (One Moon Scientific). $R_{2,eff}$ was calculated using the equation:

$$R_{2,eff}=-1/T_{CP}\ln(I_{\nu_{CPMG}}/I_0)$$

Here I_0 is the peak volume of an individual cross-peak in the spectrum recorded without CPMG delay and $I_{\nu_{CPMG}}$ corresponds to the intensity of the same cross-peak at a particular CPMG frequency.

We have then selected residues displaying non-flat relaxation dispersion profiles by visual selection for global fitting of the data. Fitting of a two-state exchange model to the data was done using the program ChemEx (version 0.6.0).[22] The software was developed by Guillaume Bouvignies and is available on `https://github.com/gbouvignies/chemex`. Amide CPMGs were fit using the n_trosy method, which is suited to analyze ^{15}N TROSY CPMG data. The ch3_mq method was applied for the methyl data.

Jackknife analysis

We investigated whether the CPMG RD data of the individual residues can be described by a single global exchange process. An often employed approach consists of comparing the exchange parameters obtained when fitting the data of single residues. In principle, if all residues sense the same process, such fits should reveal identical exchange parameters for each residue. However, it is known that fitting three parameters ($|\Delta\omega|$, k_{ex} and p_B) to data from a single residue, even when measured at multiple magnetic field strenghts, produces large uncertainties. This is particularly true when studying large systems, using the inherently less sensitive 3D HNCO approach that we needed to use to obtain sufficient resolution. We, thus, opted for a different strategy to assess whether the different residues undergo the same exchange process, based on a jackknife procedure. A pool of residues showing non-flat relaxation dispersion profiles was randomly sampled taking 60-70% of residues for fitting. The sampling was performed by in-house scripts. Typically between 50 to 500 sets of randomly grouped residues were taken and each fitted with ChemEx to a two state exchange model. The similarity of exchange parameters, reported in Figure S18, suggests that a global exchange model indeed describes the experimental data satisfactorily. Representative results of the jackknife analyses are presented in Figure S18.

Molecular dynamics simulations

Two initial molecular samples were built starting from the crystallographic structure of yAAC3 (PDB:4C9Q)[23] and of the bovine AAC (PDB:1OKC)[24] from which the specific inhibitor CATR and the cardiolipins were removed. Residues for which the position was not determined in the experiment were added using Modeller (version 9.17).[25] To model the self-aggregation of DPC around AAC, we followed a strategy employed previously to model the uncoupling protein UCP2 in DPC.[26] A solution of of DPC was prepared by positioning randomly 300 DPC molecules around yAAC3 and the bovine AAC using Packmol.[27] The overall molecular assays, neutralized with chloride anions, contains ca. 111,500 atoms embedded in a cubic box (edge 110 Å). MD simulations were carried out using the program NAMD.[28] Setup, analyses and molecular rendering were performed using VMD.[29] All trajectories were carried out in the isobaric-isothermal ensemble, at 300 K under 1 atm using, respectively, Langevin dynamics[30] (damping coefficient 1 ps^{-1}) and the Langevin piston method.[31] Long-range electrostatic interactions were taken into account by means of the Particle Mesh Ewald (PME) algorithm.[32] The Rattle algorithm was used to constrain covalent bonds involving hydrogen atoms to their equilibrium length.[33] A multiple time-step algorithm was employed to integrate the classical equations of motion with a time step of 2 and 4 fs for short- and long-range interactions, respectively.[34] The CHARMM force-field,[35] including CMAP[36] corrections, was employed to model AAC, DPC detergents and counter-ions. We first performed a MD simulation of the bovine AAC in DPC. Aggregation of DPC around the protein was first monitored over a preliminary 50 ns MD simulation during which the protein heavy atoms were harmonically restrained to their position in the crystal. Restraints were then removed in a stepwise fashion over 5 ns, and the MD simulation was extended further up to 700 ns. Aggregation of DPC around the yAAC3 was first monitored over a preliminary

35 ns MD simulation using the same protocol as for the bovine AAC. Restraints were then removed in a stepwise fashion over 5 ns, and the MD simulation was extended further up to 100 ns. For yAAC3, we employed the prediction program TALOS^{+}[37] to infer protein ϕ and ψ torsional angles from NMR chemical shits. We selected only (ϕ,ψ) angles for which prediction was unambiguous (qualified as "Good" by TALOS^{+}), resulting in a subset of 184 pairs of torsional angles (see SI Table). In order to gain insights into the structure of yAAC3 in DPC, starting from the unrestrained simulation, we produced an additional 100 ns MD trajectory during which each of the 184 (ϕ,ψ) angles was restrained to the value predicted by TALOS^{+}, by means of a weak harmonic potential (force constant of 0.1 kcal/mol/deg^2) using the colvar module of NAMD.[38] Finally, the latter restraints were entirely removed, and the dynamics of the protein surrounded by DCP was followed over 950 ns. The aggregate simulation time in this contribution amounts to *ca.* 2.0 µs.

Table S1: Exchange parameters of GGC1, ORC1 and AAC3$^{\ominus\text{c-saltbridge}}$, as determined from a global fit of CPMG RD profiles from multiple residues, measured at multiple B_0 field strengths, as indicated. Unless denoted as "2D", all data sets were collected from a series of 3D BEST-TROSY HNCO CPMG experiments, while those indicated as "2D" were obtained with 2D BEST-TROSY HN CPMG experiments. With few exceptions (AAC3, GGC1 ^{13}C ALV and GGC1$^{2\text{P}\rightarrow 2\text{R}}$+CL data) all reported error bars were determined from Jackknife analyses, cf Figure S18; these error margins were very similar to those determined by ChemEx, i.e. the method of estimation of error bars appears inconsequential.

Protein sample	nucleus	exchange rate [s^{-1}]	population[%]	number of fitted residues	field strength [^{1}H Larmor freq.]	2D or 3D	Figure
GGC1	^{15}N	1160±130	1.9± 0.3	26	700, 850	3D	S7
GGC1^{a}	^{13}C (ALV)	1160± 80	19 ± 13	7	600, 850	2D	S8
GGC1 + GTP^{b}	^{15}N	1390 ± 120	3.3± 1.2	19	600, 850	3D	S9, S10
GGC1$^{2\text{P}\rightarrow 2\text{R}}$	^{15}N	1490 ± 130	3.4± 1.2	24	600, 850	3D	S12,S13
GGC1 + cardiolipin	^{15}N	520 ± 140	9.6± 3.4	16	600, 700, 850	2D (850), 3D (600,700)	S11
GGC1 + cardiolipin + GTP	^{15}N	390 ± 110	4.5± 0.8	16	700, 850	2D (850), 3D (700)	S15
GGC1$^{2\text{P}\rightarrow 2\text{R}}$ + cardiolipin	^{15}N	480 ± 60	5.3± 0.7	10	600, 850	2D	S15
AAC3^{c}	^{15}N	1500 ± 170	1.2± 0.6	10	600, 700	3D	S14
AAC3$^{\ominus\text{c-saltbridge}\,d}$	^{15}N	1200 ± 250	1.2 (fixed)	11	600, 950	2D	S14
ORC1	^{15}N	1030 ± 600	1.1± 0.8	14	600, 850	3D	S16

---

[a] When fitting the methyl data freely, the error margin of the fitted population p_B is very substantial, even though the data quality is good (Figure S8). In a fit where p_B was fixed to 3%, very similar fit quality was obtained, with an exchange rate of 1200 s^{-1}.

[b] The population, p_B=3.3±1.2%, is slightly larger then in the apo GGC1 sample, but chemical-shift differences $|\Delta\delta|$ are smaller, and the observed small differences are thus likely due to the known problem of accurately disentangling $|\Delta\delta|$ from p_B in the fast exchange regime.[39] See Figure S9B.

[c] The original data, from reference,[4] were kindly provided by Dr. Sven Brüschweiler (University of Vienna), and fitted identically to all other data in this study.

[d] p_B was fixed to the value found for WT AAC3, to improve the convergence (i.e. the precision of the obtained k_{ex}.

Table S2: Substrate transport assays of MCs performed in proteoliposomes on wild-type and mutant proteins. Details of these experiments are provided in the materials and methods section in the Supporting Information above.

Protein	Transport rate [nmol · mg protein^{-1} · 5 min]	residual activity
AAC3	630 ± 31.5	
AAC3$^{\ominus\text{c-saltbridge}}$	4.7 ± 0.3	0.7 ± 0.05 %
GGC1	1200 ± 37	
GGC1$^{2\text{P}\rightarrow 2\text{R}}$	26 ± 4	2.1 ± 0.4 %

Table S3: Nucleotide transport specificity of GGC1 and AAC3 in liposome transport assays. GGC1 or AAC3 were reconstituted in liposomes (see Methods section), which were preloaded with internal nucleotide ("[nucleotide$_{\text{in}}$]) and externally added nucleotide ("[nucleotide$_{\text{out}}$]), as indicated in the table. The uptake of radioactively labeled GTP or ATP into liposomes was measured under these different conditions. These data establish that GGC1 specifically transports GTP, not ATP, and this transport is not inhibited significantly by externally added ATP, and likewise AAC3 is specific for ATP.

GGC1						
$[\text{GDP}]_{\text{in}}$	$[\text{ATP}]_{\text{in}}$	^{3}H-$[\text{GTP}]_{\text{out}}$	$[\text{ATP}]_{\text{out}}$	transport rate [µmol · mg protein^{-1} · 2 min]	residual activity	
5 mM		50 µM		0.67 ± 0.044	100%	
	5 mM	50 µM		0.0056 ± 0.00028	0.8%	no significant ATP transport
5 mM		50 µM	150 µM	0.6 ± 0.0331	89%	no significant inhibition by ATP

AAC3						
$[\text{ATP}]_{\text{in}}$	$[\text{GTP}]_{\text{in}}$	^{3}H-$[\text{ATP}]_{\text{out}}$	$[\text{GTP}]_{\text{out}}$	transport rate [µmol · mg protein^{-1} · 2 min]	residual activity	
5 mM		10 µM		0.35 ± 0.0157	100%	
	5 mM	10 µM		0.027 ± 0.00105	7.7%	no significant GTP transport
5 mM		10 µM	150 µM	0.36 ± 0.01433	102%	no significant inhibition by GTP

Table S4: List of 184 (ϕ,ψ) torsional angles (°) from TALOS$^+$, used for restraining the MD simulation, and corresponding dihedral angles from the crystal structure (PDB 4C9Q, chain A). See Supplementary Methods section for details about the implementation of the restraints in MD. Table continued on next page.

TALOS$^+$			Crystal structure			TALOS$^+$			Crystal structure		
Residue	ϕ	ψ	Residue	ϕ	ψ	Residue	ϕ	ψ	Residue	ϕ	ψ
T10	-68.42	-32.08	T10	-63.8	-41.0	E70	-67.98	-29.03	E70	-112.8	-41.4
N11	-69.42	-34.06	N11	-61.8	-44.0	G71	-68.44	-32.40	G71	127.8	-170.8
F12	-67.36	-34.29	F12	-66.9	-33.0	L72	-64.56	-39.94	L72	-88.0	-36.6
A13	-63.58	-40.56	A13	-69.7	-45.1	I73	-64.63	-37.39	I73	-69.5	-21.0
I14	-61.88	-43.69	I14	-65.4	-40.8	S74	-65.25	-40.18	S74	-67.0	-15.1
N15	-64.27	-35.29	N15	-62.3	-37.9	F75	-67.07	-38.25	F75	-74.6	-7.5
F16	-65.13	-39.97	F16	-69.0	-49.4	W76	-68.20	-33.87	W76	-108.6	13.8
L17	-64.02	-40.56	L17	-65.5	-48.0	R77	-80.08	-13.13	R77	-67.7	113.9
M18	-96.17	1.97	M18	-66.2	-26.9	T80	-60.80	-36.70	T80	-59.6	-36.9
G19	84.64	5.12	G19	-64.6	-37.9	A81	-63.96	-35.10	A81	-58.4	-44.1
V21	-60.13	-41.17	V21	-63.3	-45.9	N82	-65.40	-36.91	N82	-64.7	-36.2
S22	-61.82	-39.29	S22	-58.6	-45.5	V83	-64.37	-38.86	V83	-66.5	-49.6
A23	-66.20	-39.08	A23	-65.4	-39.7	I84	-65.90	-32.06	I84	-64.5	-42.0
A24	-65.40	-39.59	A24	-61.9	-45.9	R85	-66.47	-29.13	R85	-54.9	-23.0
I25	-68.22	-36.04	I25	-66.9	-43.2	Y86	-94.26	-5.16	Y86	-57.9	-54.3
A26	-65.64	-33.70	A26	-58.7	-46.3	F87	-84.91	122.46	F87	-61.6	-47.9
K27	-76.86	-24.49	K27	-74.0	-32.2	P88	-61.66	145.65	P88	-70.0	-27.2
S31	-82.52	135.13	S31	-70.1	-44.1	T89	-59.58	-27.09	T89	-69.6	-55.4
P32	-53.82	-31.77	P32	-59.5	-46.3	Q90	-67.29	-28.41	Q90	-66.7	-32.6
I33	-68.51	-36.79	I33	-62.4	-31.5	A91	-72.23	-21.50	A91	-62.4	-42.3
E34	-60.91	-45.59	E34	-65.8	-44.3	L92	-85.82	-15.23	L92	-70.5	-36.1
R35	-64.03	-38.62	R35	-66.9	-35.5	A95	-64.67	-30.36	A95	-93.9	-49.2
V36	-65.35	-41.68	V36	-61.1	-40.4	F96	-69.41	-33.23	F96	-118.3	-18.2
K37	-60.49	-44.02	K37	-59.6	-49.9	K97	-61.84	-41.31	K97	-60.1	-40.2
I38	-63.43	-41.12	I38	-64.1	-35.0	D98	-64.05	-41.20	D98	-69.9	-35.9
L39	-64.18	-41.42	L39	-68.9	-48.7	K99	-66.85	-42.01	K99	-67.7	-39.3
I40	-66.50	-37.08	I40	-65.3	-38.3	I100	-64.68	-43.78	I100	-65.6	-37.8
Q41	-70.46	-35.02	Q41	-66.7	-41.6	K101	-61.30	-41.33	K101	-65.3	-33.5
N42	-60.46	-44.70	N42	-113.5	34.	L102	-71.45	-34.96	L102	-78.8	-14.6
I47	-63.50	-33.34	I47	-63.4	-41.8	Y112	-61.02	-33.30	Y112	-68.9	-39.4
K48	-69.26	-30.95	K48	-63.1	-45.9	G113	-61.29	-41.91	G113	-63.3	-43.1
K54	-61.66	-40.46	K54	-125.8	151.	K114	-67.53	-37.08	K114	-73.1	-31.1
K55	-68.92	-29.92	K55	-62.7	142.2	W115	-65.25	-38.10	W115	-71.7	-34.9
Y56	-71.24	-33.31	Y56	-68.5	127.8	F116	-69.70	-32.23	F116	-64.3	-49.2
S57	-60.11	-36.02	S57	-74.1	-19.8	A117	-78.14	-17.21	A117	-63.3	-37.1
G58	-66.56	-39.42	G58	170.6	-163.5	A125	-61.51	-35.88	A125	-65.7	-45.1
I59	-72.06	-35.53	I59	-69.2	-46.7	A126	-66.19	-37.34	A126	-63.0	-43.9
V60	-62.03	-43.88	V60	-62.0	-45.5	G127	-64.94	-39.45	G127	-62.5	-47.5
D61	-61.77	-41.47	D61	-61.5	-39.9	A128	-66.34	-39.22	A128	-65.2	-44.0
A62	-64.26	-37.70	C62	-62.8	-44.4	L129	-64.14	-40.72	L129	-61.8	-39.9
F63	-65.94	-42.12	F63	-60.6	-49.7	S130	-66.44	-34.77	S130	-69.4	-40.4
K64	-65.20	-42.72	K64	-60.9	-51.6	L131	-65.97	-31.88	L131	-64.1	-23.9
R65	-68.47	-37.02	R65	-62.3	-45.5	L132	-72.06	-25.04	L132	-57.3	-33.6
T66	-63.04	-35.60	T66	-63.9	-42.6	F133	-78.20	-39.70	F133	-104.2	-21.0
A67	-70.73	-29.48	A67	-68.1	-39.2	F139	-63.69	-39.06	F139	-58.2	-52.4
K68	-84.80	-15.54	K68	-75.8	-32.8	A140	-64.43	-44.20	A140	-61.9	-34.2

Continued: List of 184 (ϕ,ψ) torsional angles (°) from TALOS$^+$, used for restraining the MD simulation, and corresponding dihedral angles from the crystal structure (PDB 4C9Q, chain A).

TALOS$^+$			Crystal structure			TALOS$^+$			Crystal structure		
Residue	ϕ	ψ	Residue	ϕ	ψ	Residue	ϕ	ψ	Residue	ϕ	ψ
R141	-61.92	-44.31	R141	-59.2	-51.2	N255	-60.40	-31.06	N255	-89.4	51.7
T142	-68.54	-39.38	T142	-63.5	-46.6	G256	-65.64	-36.40	G256	116.7	168.2
R143	-66.97	-23.70	R143	-64.2	-37.6	A257	-67.00	-38.17	A257	-68.8	-38.3
L144	-80.20	-19.07	L144	-70.7	-34.0	I258	-64.18	-43.31	I258	-65.5	-43.8
A145	-98.83	6.64	A145	-76.0	-17.5	D259	-63.40	-39.93	D259	-62.3	-42.2
L162	-63.98	-37.37	L162	-64.8	-51.0	A260	-64.87	-40.87	C260	-61.5	-46.2
T163	-64.47	-39.86	T163	-73.8	-23.3	L261	-62.74	-43.39	L261	-59.4	-45.1
D164	-65.46	-40.54	D164	-65.7	-36.1	K262	-60.83	-41.78	K262	-62.7	-45.7
V165	-66.44	-39.19	V165	-57.8	-48.2	K263	-64.58	-40.88	K263	-66.4	-37.2
Y166	-65.50	-42.71	Y166	-58.5	-47.7	I264	-65.84	-39.01	I264	-62.8	-49.2
K167	-62.73	-36.08	K167	-60.2	-50.9	V265	-70.77	-25.91	V265	-62.7	-43.3
K168	-68.86	-29.88	K168	-71.0	-35.3	A266	-82.55	-15.49	A266	-69.3	-27.4
T169	-63.09	-36.94	T169	-69.0	-43.3	S267	-70.09	-27.23	S267	-97.3	-42.7
L170	-70.01	-26.12	L170	-67.3	-35.5	E268	-88.98	-6.11	E268	-121.2	-13.7
K171	-86.59	-9.33	K171	-69.5	-28.7	V270	-61.38	-35.55	V270	-66.7	-35.9
D173	-92.53	-4.49	D173	-113.8	-22.6	G271	-61.27	-40.34	G271	-59.0	-26.1
G174	82.80	18.77	G174	92.2	-153.9	S272	-64.25	-39.22	S272	-65.1	-20.2
I175	-66.80	-34.30	I175	-71.8	-24.4	L273	-71.13	-31.40	L273	-74.8	-16.7
A176	-66.08	-30.09	A176	-63.9	-36.4	F274	-83.86	-12.42	F274	-108.5	22.6
G177	-66.29	-34.53	G177	-64.0	-28.6	K275	-82.65	-7.91	K275	-73.0	119.6
L178	-69.08	-34.37	L178	-76.8	-23.4	G276	88.65	18.81	G276	93.0	6.5
Y179	-66.68	-33.75	Y179	-111.6	47.0	A277	-66.40	-24.69	C277	-66.1	-44.7
R180	-71.40	-29.14	R180	-83.7	121.1	G278	-62.78	-42.32	G278	-65.0	-38.2
Y196	-61.82	-40.38	Y196	-62.0	-56.9	A279	-65.78	-39.07	A279	-64.2	-32.3
F197	-70.12	-40.79	F197	-67.3	-36.1	N280	-68.68	-38.02	N280	-69.4	-37.5
D201	-60.25	-42.38	D201	-67.2	-36.7	I281	-65.56	-38.93	I281	-64.3	-42.0
S202	-64.67	-36.85	S202	-67.9	-36.7	L282	-62.02	-42.11	L282	-61.9	-38.3
L203	-78.76	-31.42	L203	-96.2	2.1	R283	-63.42	-41.33	R283	-63.8	-35.9
G214	-60.91	-29.71	K204	-62.3	-47.8	S284	-64.88	-31.59	S284	-64.6	-48.9
S215	-65.13	-37.90	P205	-67.0	-18.5	V285	-69.07	-26.35	V285	-68.6	-26.8
F216	-65.39	-42.67	F216	-	-	G289	85.41	12.17	G289	-63.0	-52.4
L217	-63.62	-43.00	L217	-64.7	-46.8	V290	-68.14	-35.36	V290	-72.2	-23.8
A218	-59.57	-41.54	A218	-62.1	-41.5	I291	-66.41	-37.42	I291	-78.7	-26.0
S219	-65.87	-38.36	S219	-64.7	-43.8	S292	-63.45	-44.64	S292	-74.5	-43.2
F220	-64.48	-39.31	F220	-65.4	-42.6	M293	-62.92	-40.41	M293	-59.8	-44.5
L221	-75.53	-30.25	L221	-64.5	-38.0	Y294	-65.31	-37.84	Y294	-68.3	-30.6
L237	-63.92	-36.69	L237	-66.1	-36.1	D295	-64.95	-37.56	D295	-62.7	-40.4
D238	-68.11	-34.25	D238	-69.2	-39.2	Q296	-66.63	-38.70	Q296	-68.2	-40.7
T239	-66.18	-39.21	T239	-62.0	-48.0	L297	-62.87	-44.35	L297	-64.3	-40.2
V240	-65.52	-43.50	V240	-59.6	-43.1	Q298	-63.19	-40.52	Q298	-69.8	-32.1
R241	-62.40	-42.18	R241	-56.0	-52.5	M299	-62.68	-41.61	M299	-66.2	-27.9
R242	-61.99	-42.11	R242	-66.5	-39.6	I300	-66.27	-43.42	I300	-82.8	-50.6
R243	-65.05	-33.62	R243	-69.2	-25.1	L301	-64.98	-25.38	L301	-66.6	-61.2
M244	-64.86	-34.52	M244	-76.1	-29.4	F302	-100.66	1.62	F302	-97.7	163.5
M245	-67.01	-30.86	M245	-65.6	-34.1	G303	98.46	6.16	G303	-64.3	-41.2
M246	-77.15	-19.40	M246	-68.4	-26.2	F306	-85.63	120.50	F306	-	-

Table S5: ^{1}H-^{15}N-^{13}CO frequency list of the assigned residues in yORC1; the ^{13}CO frequency corresponds to the residue i-1.

Residue	ωH (ppm)	ωC' (ppm)	ωN (ppm)	Residue	ωH (ppm)	ωC' (ppm)	ωN (ppm)
12Asp	8.43	-	121.91	182Ser	8.53	177.71	116.12
13Ser	8.27	176.57	116.46	183Gly	8.21	175.66	109.72
14Lys	8.26	174.91	122.78	184Thr	7.99	175.44	116.78
15Lys	8.16	176.80	121.76	201Ile	7.73	179.37	119.67
16Lys	8.26	176.61	122.12	202Val	8.19	178.79	122.23
17Gly	8.55	177.20	109.22	203Lys	8.43	177.49	119.22
18Leu	8.55	174.71	122.38	204Lys	7.83	178.51	117.79
19Ile	8.36	178.73	118.21	205Ser	7.89	178.36	114.53
20Glu	8.73	176.69	120.51	206Leu	7.87	176.15	119.55
21Gly	8.23	177.74	105.74	207Lys	7.85	178.34	119.27
22Ala	7.98	174.94	123.71	208Asp	8.25	177.90	119.31
23Ile	8.23	179.75	117.13	209Arg	7.80	177.07	119.30
24Leu	8.06	177.68	119.70	210His	8.22	176.50	117.74
25Asp	7.96	178.77	118.31	211Ser	8.16	174.90	115.86
26Ile	7.86	179.39	120.42	212Leu	8.26	175.56	122.43
27Ile	8.20	178.58	119.60	213Asp	8.04	176.84	119.79
28Asn	8.45	177.06	117.01	214Asp	8.12	175.39	121.26
29Gly	8.08	177.28	107.14	218Asp	8.31	176.14	121.10
30Ser	8.16	175.28	116.90	219Glu	8.45	176.37	121.03
31Ile	8.16	175.43	120.53	220Ser	8.50	176.74	116.41
32Ala	8.22	176.80	123.14	221Lys	8.50	175.65	124.12
33Gly	8.24	179.76	106.09	222Ile	8.20	178.28	119.30
34Ala	8.02	175.36	123.13	224Glu	7.82	177.44	116.61
35Cys	8.24	178.56	114.51	227Ile	7.84	177.96	114.45
36Gly	8.20	175.69	107.57	228Ser	8.00	177.56	115.87
37Lys	7.78	174.37	118.88	229Gly	8.35	176.19	110.04
38Val	7.91	177.00	118.15	230Gly	8.33	174.96	108.05
81Gly	8.40	177.08	108.14	231Ser	8.23	174.48	115.40
87Val	7.88	178.75	117.99	232Ala	8.18	175.22	123.88
88Gly	8.36	177.97	106.66	233Gly	8.16	178.50	105.72
89Ala	7.89	175.65	122.62	234Leu	7.87	174.32	120.44
90Cys	8.04	179.97	116.53	235Ala	7.93	176.67	121.91
94Ala	8.16	175.69	122.64	236Phe	8.03	177.16	117.70
95Thr	7.92	178.40	109.32	237Asn	8.05	175.14	118.84
96Leu	7.86	175.53	121.25	238Ala	8.31	174.77	122.70
117Gly	8.25	178.28	106.21	239Ser	8.21	177.71	113.15
122Ser	8.14	177.06	116.92	240Ile	7.56	174.61	117.89
123Gly	8.33	175.44	109.47	241Phe	7.80	174.86	119.71
124Gly	8.19	174.58	107.80	243Ala	8.55	176.80	126.14
125Val	8.14	174.62	119.11	244Asp	8.68	178.88	116.40
126Ala	8.48	176.53	124.50	245Thr	7.83	178.24	116.97
127Gly	8.35	178.62	106.41	246Val	7.92	175.82	120.40
128Ser	8.10	175.26	116.16	248Ser	7.86	178.36	113.49
129Cys	8.44	175.60	119.77	249Val	7.96	176.79	120.38
147Ala	8.08	176.72	123.58	258Thr	8.41	178.51	112.71
148Asn	8.12	177.90	115.73	282Phe	7.82	176.64	115.23
149Leu	8.05	175.74	120.88	283Arg	7.96	175.72	119.23
150Gln	8.23	177.57	119.73	284Ala	8.16	175.78	123.62
166Lys	8.41	177.47	118.37	285Val	7.92	177.10	119.61
167Ala	7.83	178.43	121.53	287Ala	8.31	176.40	123.50
169Ile	8.04	177.90	117.51	288Asn	8.29	177.44	117.38
170Thr	8.14	177.89	113.35	290Ala	7.86	174.86	127.86
171Glu	8.16	178.05	120.52	291Val	8.04	179.01	115.38
172Arg	8.21	177.97	115.45	292Phe	7.95	177.22	118.63
173Gly	8.04	177.32	107.47	293Tyr	8.16	177.41	118.89
174Leu	8.48	174.34	119.54	294Ile	8.25	179.11	120.86
175Ala	8.38	177.91	119.37	295Phe	8.30	177.24	118.99
176Gly	7.99	179.46	104.58	296Glu	8.63	178.10	119.87
177Leu	7.72	175.68	119.94	297Thr	7.80	178.97	115.62
178Trp	7.70	177.29	116.16	298Leu	8.02	176.19	118.92
179Gln	7.81	175.95	117.37	299Ser	7.72	178.00	111.57
180Gly	7.97	176.71	107.70	300Ala	7.25	173.73	122.60
181Gln	8.61	174.76	120.22	301Leu	7.17	176.72	124.13

Figure S1: Phylogenetic relationship between yeast mitochondrial carriers. AAC3 is colored in blue, GGC1 in green and ORC1 in red. The numbers indicate sequence identity between the three carries.

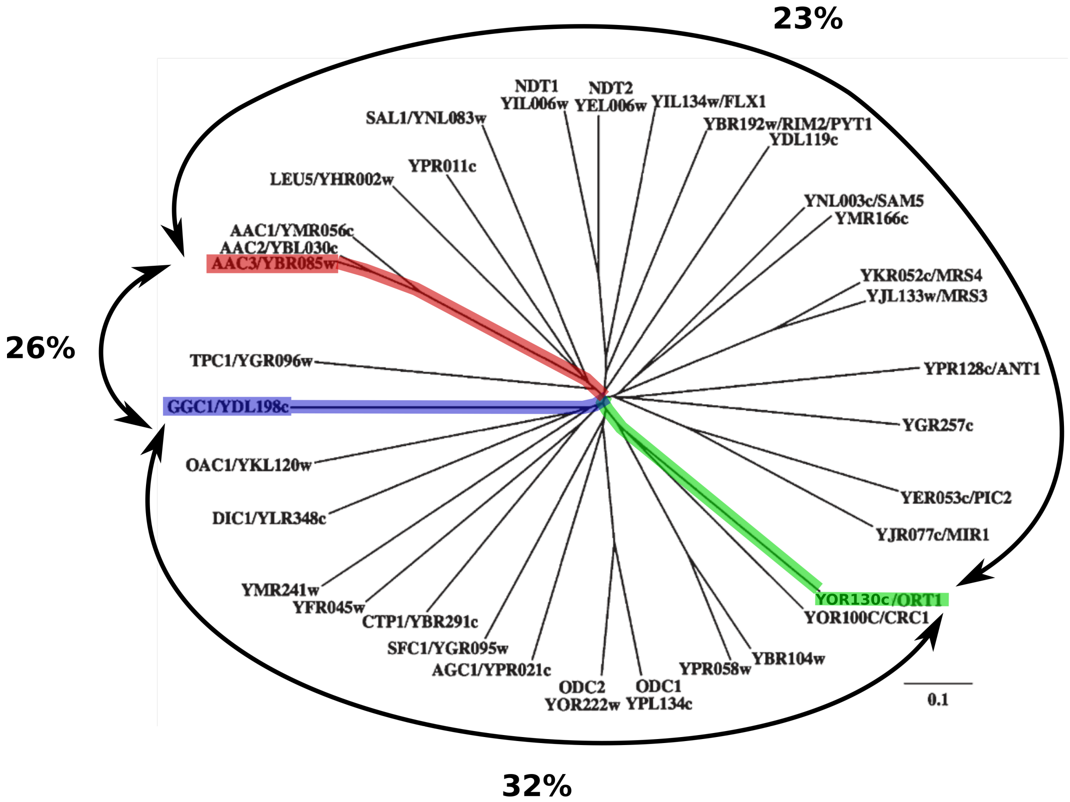

Figure S2: Samples of the three MCs are monomeric and homogeneous. (a) Representative size-exclusion chromatography profiles (top) and SDS-PAGE gels for GGC1, ORC1 and AAC3$^{\ominus\text{c-saltbridge}}$. HiLoad Superdex 200 16/60 prep grade columns were used for the two former proteins, while Superdex 10/300 GL column was used for AAC3, therefore the difference in elution volumes. Relatively sharp and symmetrical gel filtration peaks are suggestive of a homogeneous samples. Note that the contrast of SDS-PAGE gel for GGC1 was enhanced to make impurities more visible. (b) Analytical ultra-centrifugation data for GGC1 and ORC1, revealing homogeneous samples. Note that the sedimentation coefficient for GGC1 is higher as compared to ORC1. This could indicate different amounts of bound detergent.

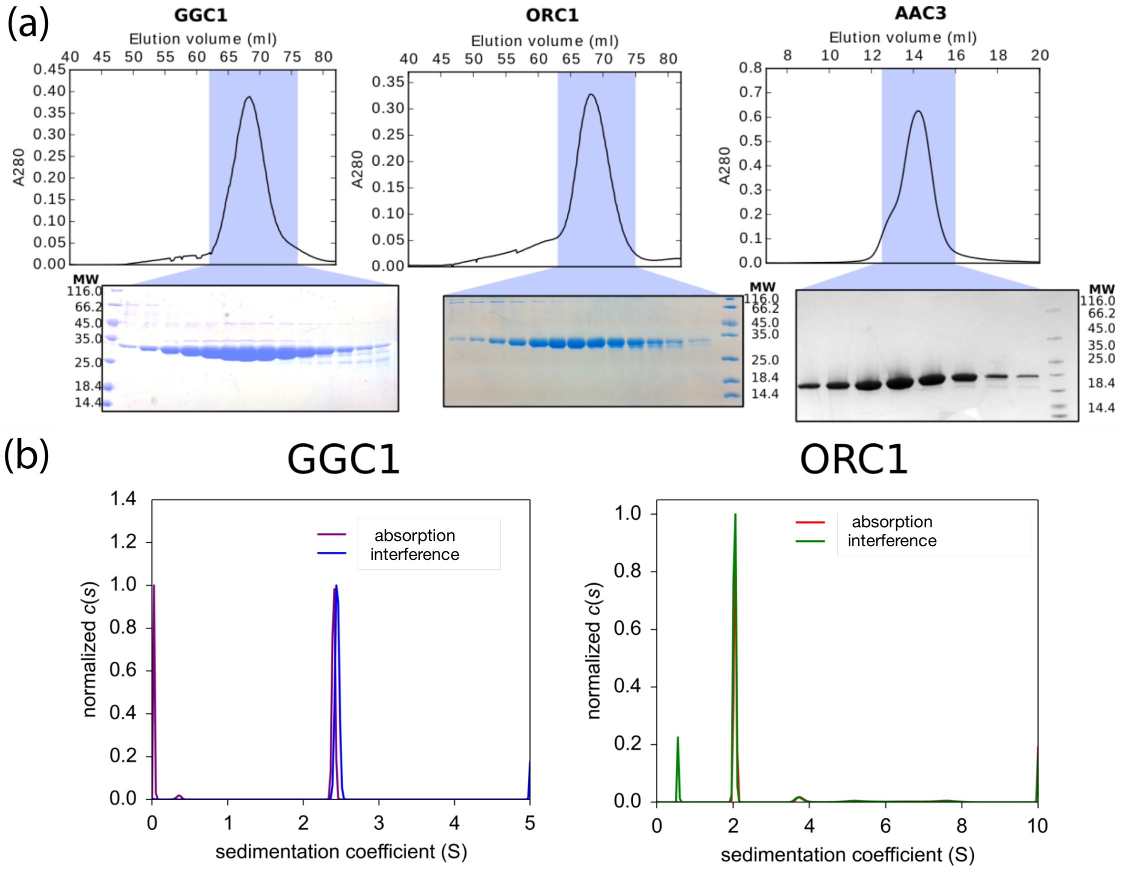

Figure S3: NMR spectra of the three MCs investigated in this study. 2D BEST-TROSY ^{1}H-^{15}N HSQC spectra of (A) GGC1, (B) AAC$^{\circleddash\text{c-saltbridge}}$ and (C) ORC1. (D) shows a temperature-series of ORC1 spectra, and (E) shows residue-wise temperature-dependent chemical-shift changes for residues in ORC1 and AAC3. The spectra were referenced according to a set of least shifting residues, so the systematic shift due to the temperature-dependent changes of hydrogen bonding can be neglected, and thus facilitate visualization of overall spectral changes. As can be seen, the spectra become less disperse in the ^{1}H dimension, indicating the loss of structure. However, all the shift magnitudes are linear, suggesting that no unfolding transition occurs. (F) shows methyl ^{1}H-^{13}C HMQC spectra of GGC1.

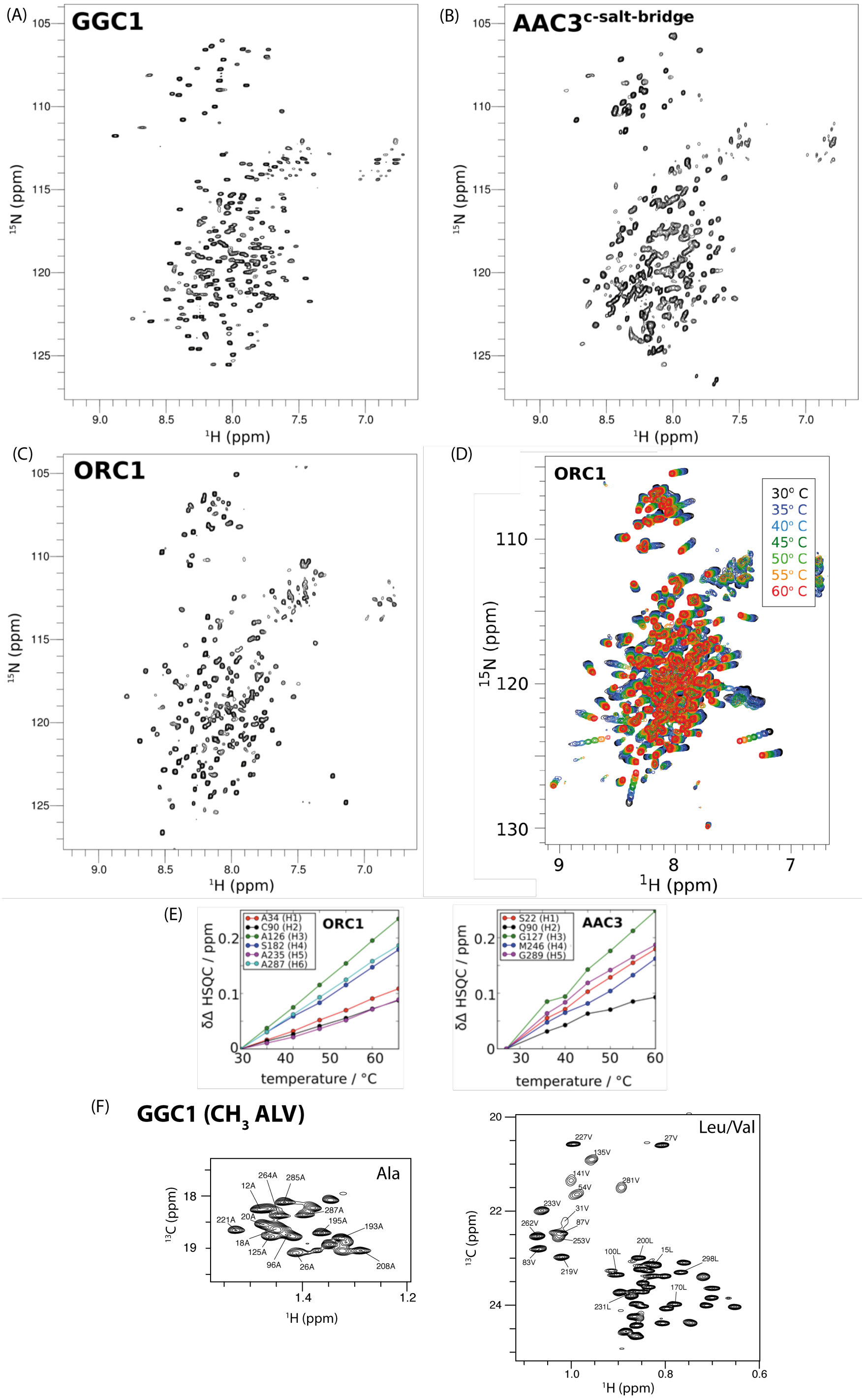

Figure S4: (A) Residue-wise likelihood of helicity in AAC3 determined by TALOS$^+$ according to the Cα, Cβ, CO, N and H chemical shifts (BMRB desposition number 26589). The color code indicates the classification, according to TALOS$^+$. Indicated on top are the positions of helices in the crystal structure of AAC3.[10] B, TALOS+-predicted order parameters. C, TALOS$^+$-determined helicity plotted onto the crystal structure, in which the loops which are not resolved in the X-ray structure have been modeled. Gray regions correspond to regions for which predictions are not available due to the lack of assignment. Spheres indicate non-flat relaxation dispersion profiles as reported by Bruschweiler et al.[4]

We also considered the possibility that TALOS$^+$, which was trained against a set of soluble protein structures, might not be accurate in DPC detergent, because DPC might have direct effects on chemical shifts. To investigate this issue, we applied TALOS$^+$ to chemical-shift data of the proteins TSPO locked by a tightly bound ligand[40] and DsbB[41] in DPC detergent. The agreement between TM helices and corresponding shifts is excellent (panel D), showing that TALOS$^+$ can reliably determine helical regions also in the presence of DPC.

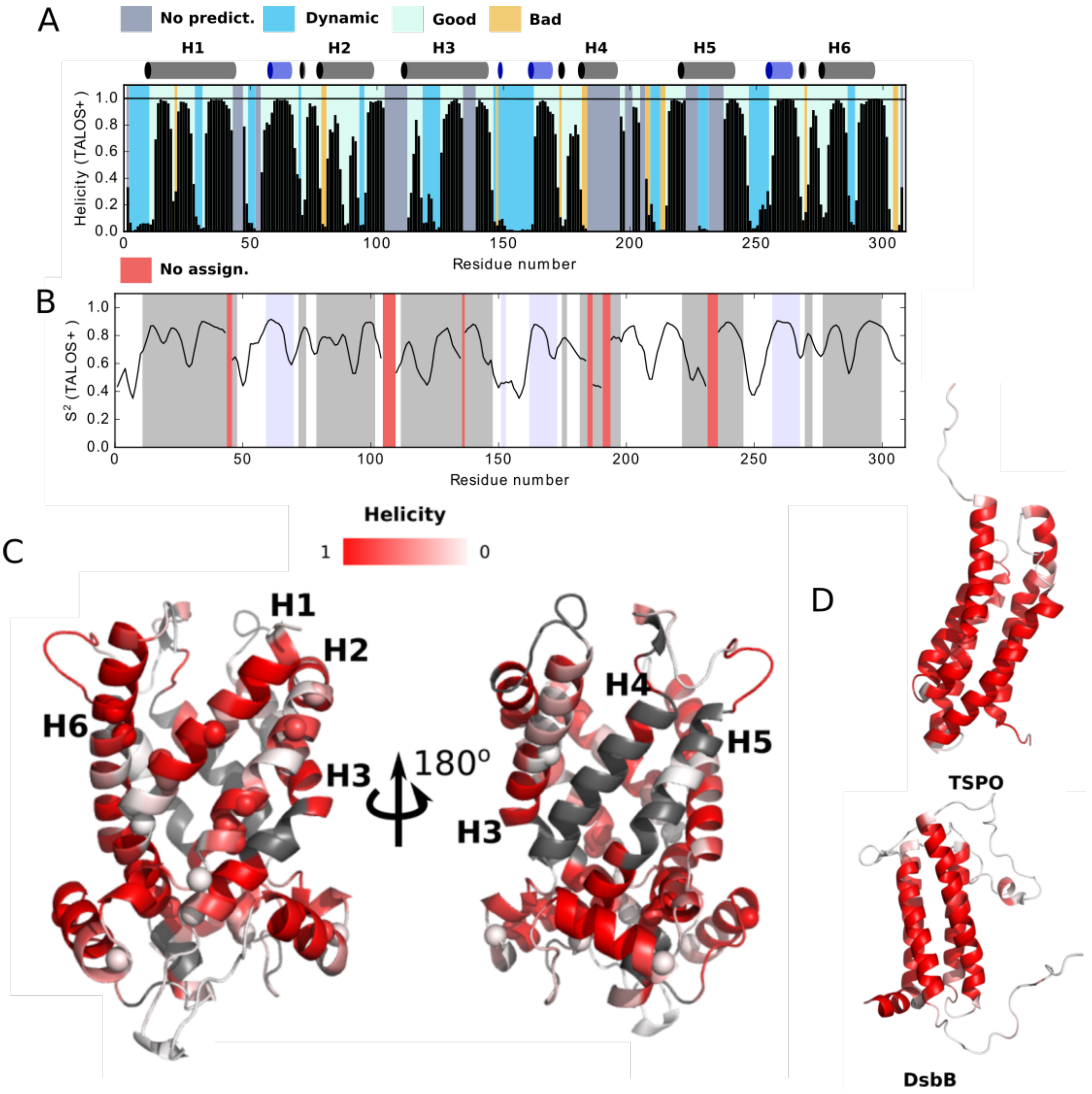

Figure S5: Residue-wise transverse relaxation rates for GGC1$^{2P \rightarrow 2R}$. The agreement is very good with the previously published data for wild-type GGC1.[11] The arrow highlights depressed R_2 rate constants in the region of H4 which also shows non-helical chemical shifts, according to TALOS+.

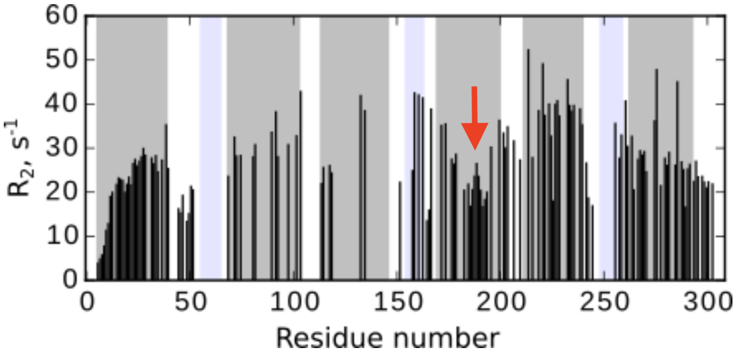

Figure S6: Hydrogen-deuterium exchange experiment with GGC1 in DPC. (A) Time-dependent decay of the amide signal of GGC1, followed by a series of one-dimensional spectra. Shown is the integral over the amide region. GGC1 in H_2O buffer was concentrated to 1 mM, and then diluted into D_2O based buffer at a ratio of 1:4 (i.e., 80% D_2O final). Due to the very fast H/D exchange, only 1D spectra could be recorded. (B) The loss of signal is not due to protein aggregation. Shown are three spectra: (i) of the initial sample in H_2O buffer (blue), (ii) of the sample in 80% D_2O buffer after ca. 1 hour (black). (iii) At the end of the HDX experiment, the sample was transferred from the 80% D_2O buffer to a H_2O buffer; this leads to a full recovery of the amide signal (the number of scans in this experiment was adjusted to account for dilution). This recovery of the initial signal shows that the signal drop in (A) is due to exchange of amide protons to deuterium, and not due to protein aggregation. To estimate the level of exchange-competent states from this 1D HDX experiment, we have used Excel sheets by the S. W. Englander lab (hx2.med.upenn.edu/download.html) to calculate the intrinsic chemical exchange rate constant, taking into account the pH (6) and temperature 30°C used experimentally. Because our measurements were done in 1D mode, we averaged the predicted rate constants over the sequence of GGC1. An exchange rate constant of 1 min^{-1} (or 2 min^{-1} or 0.5 min^{-1}) corresponds to a population of open state of 4% (or 10%, or 2%, respectively).

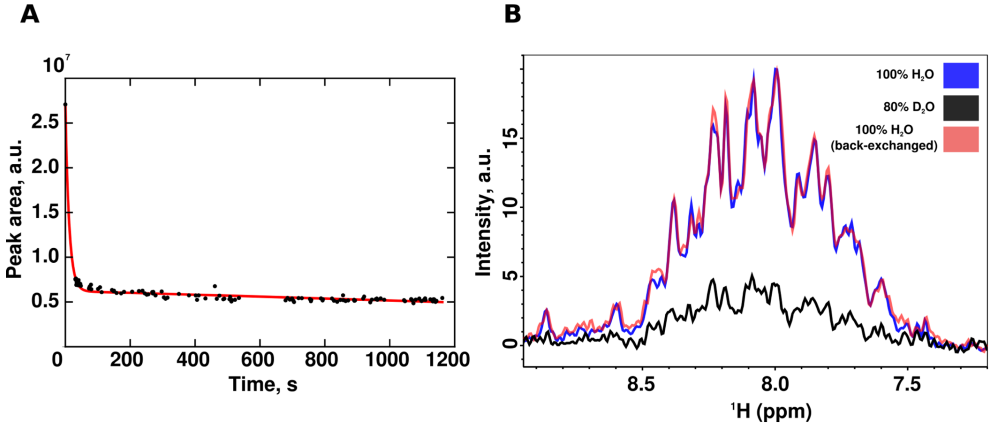

Figure S7: ^{15}N CPMG relaxation dispersion data for apo GGC1 recorded at 700 (black dots) and 850 (red dots) MHz ^{1}H Larmor frequency, and the fits corresponding to a global two-state model (dashed lines). Numbers above each panel indicate residue numbers of GGC1. All fit parameters are reported in Table S1.

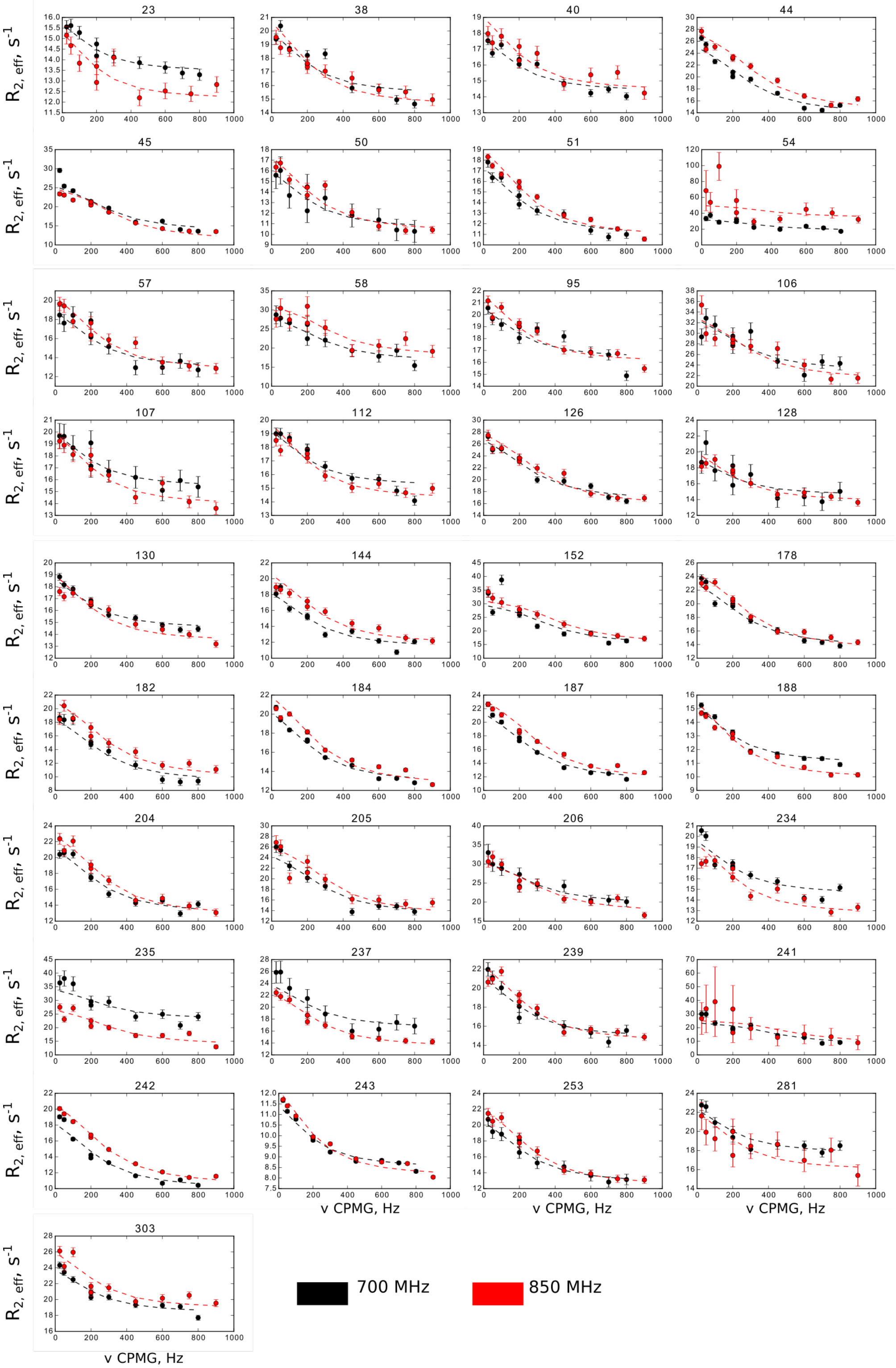

Figure S8: Methyl ^{13}C CPMG relaxation dispersion data for apo GGC1 recorded on 600 (black dots), 700 (red dots) and 850 (blue dots) MHz NMR spectrometers and the corresponding fits (dashed lines) to a global two-state model. Numbers above each panel indicate residue numbers of GGC1. (The upper left panel shows data of a Leu residue - according to its chemical shift -, for which assignment could not be obtained.)

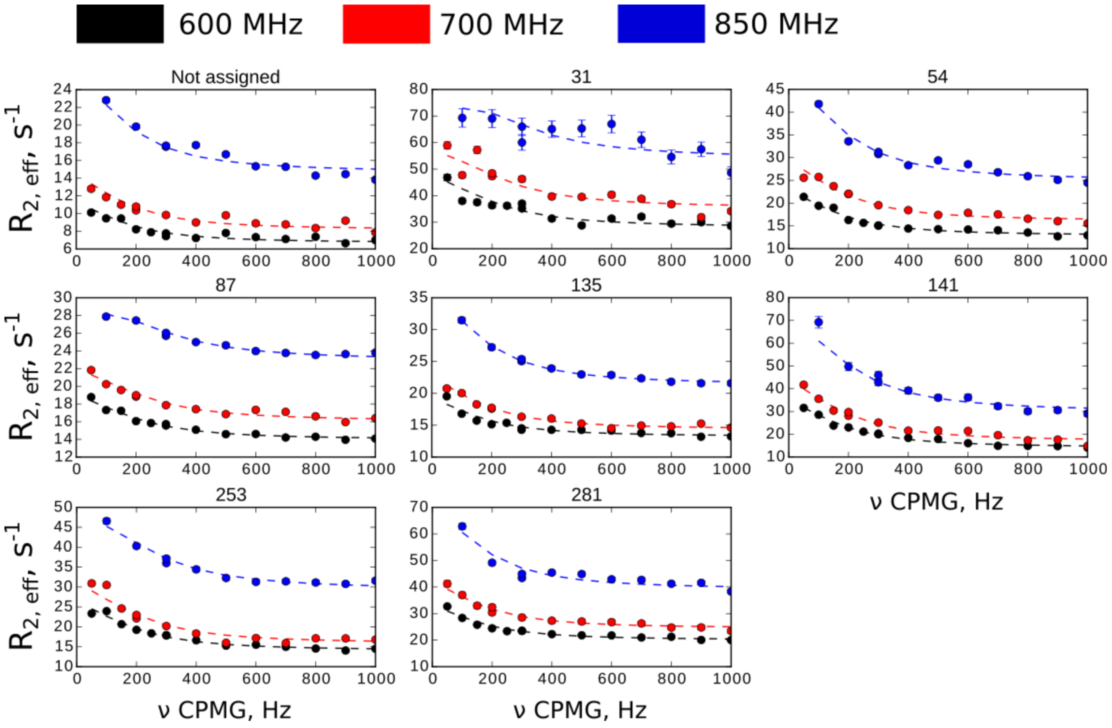

Figure S9: (A) Comparison of ^{15}N CPMG RD profiles observed for apo GGC1 (black dots) and GGC1 in the presence of 20 mM GTP (red dots) at a ^{1}H Larmor frequency of 850 MHz. Numbers above each panel correspond to the residue number in GGC1. Largest differences observed between the two samples correspond to the loops on the mitochondrial-matrix side. The dispersions corresponding to the residues in TM and mitochondrial helices are hardly affected by the presence of GTP. To facilitate the comparison of the CPMG dispersion curves, an additive offset of $R_{2,\mathrm{eff}}$ (i.e. plateau) was added to some residues. Such an offset does not have any impact on the fit results, because the plateau is not attributed any physical meaning in terms of exchange. (B) shows the fitted chemical-shift differences for these two cases. The fitted chemical-shift differences $|\Delta\delta|$ in the presence of GTP are lower, but the fitted population is higher, which at least partially compensate, such that the CPMG RD profiles are overall similar. Given the high similarity of the raw CPMG data it is very unlikely that the differences in fit parameters are statistically relevant. All fit parameters are reported in Table S1.

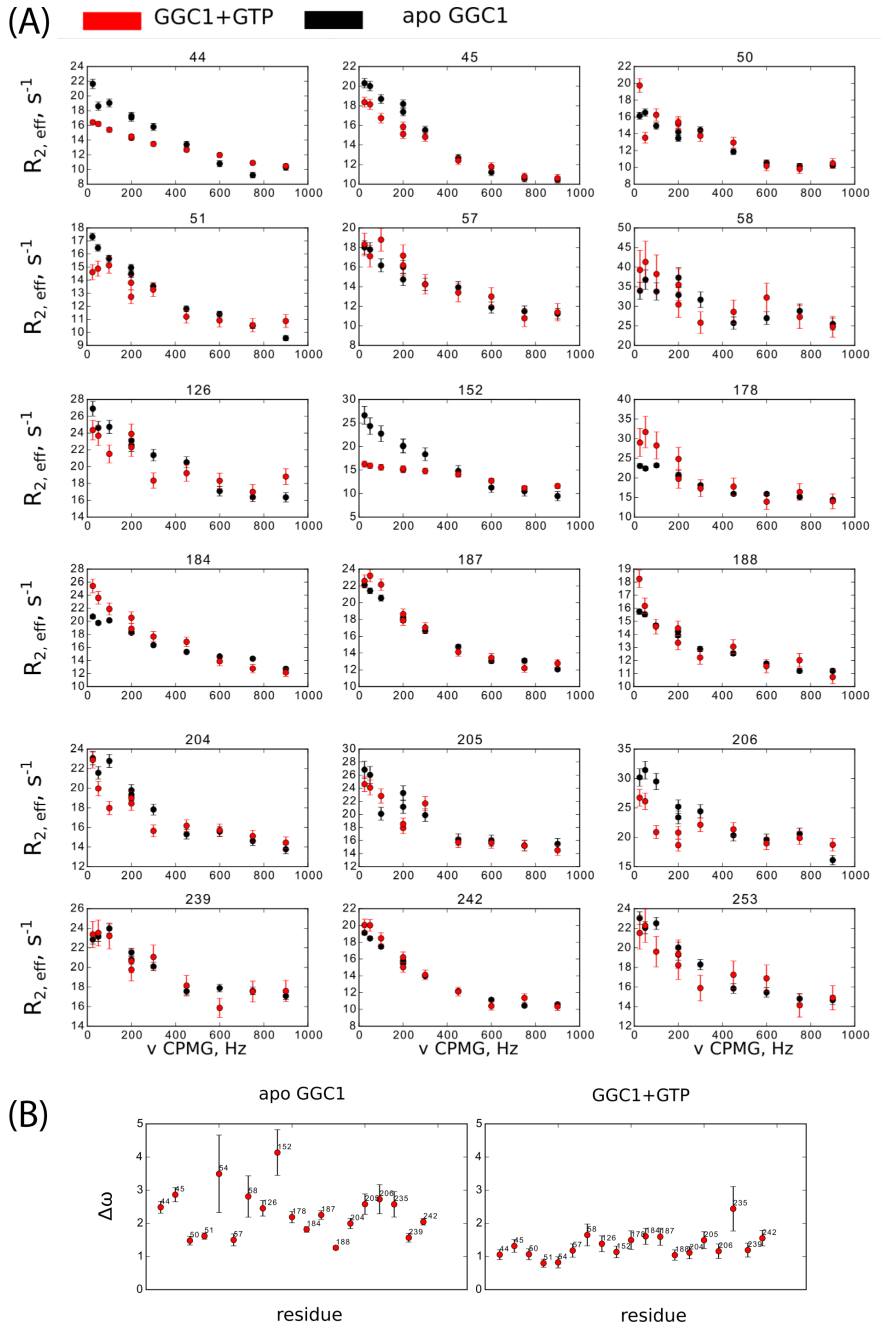

Figure S10: ^{15}N CPMG RD profiles of GGC1 in presence of GTP. All fit parameters are reported in Table S1.

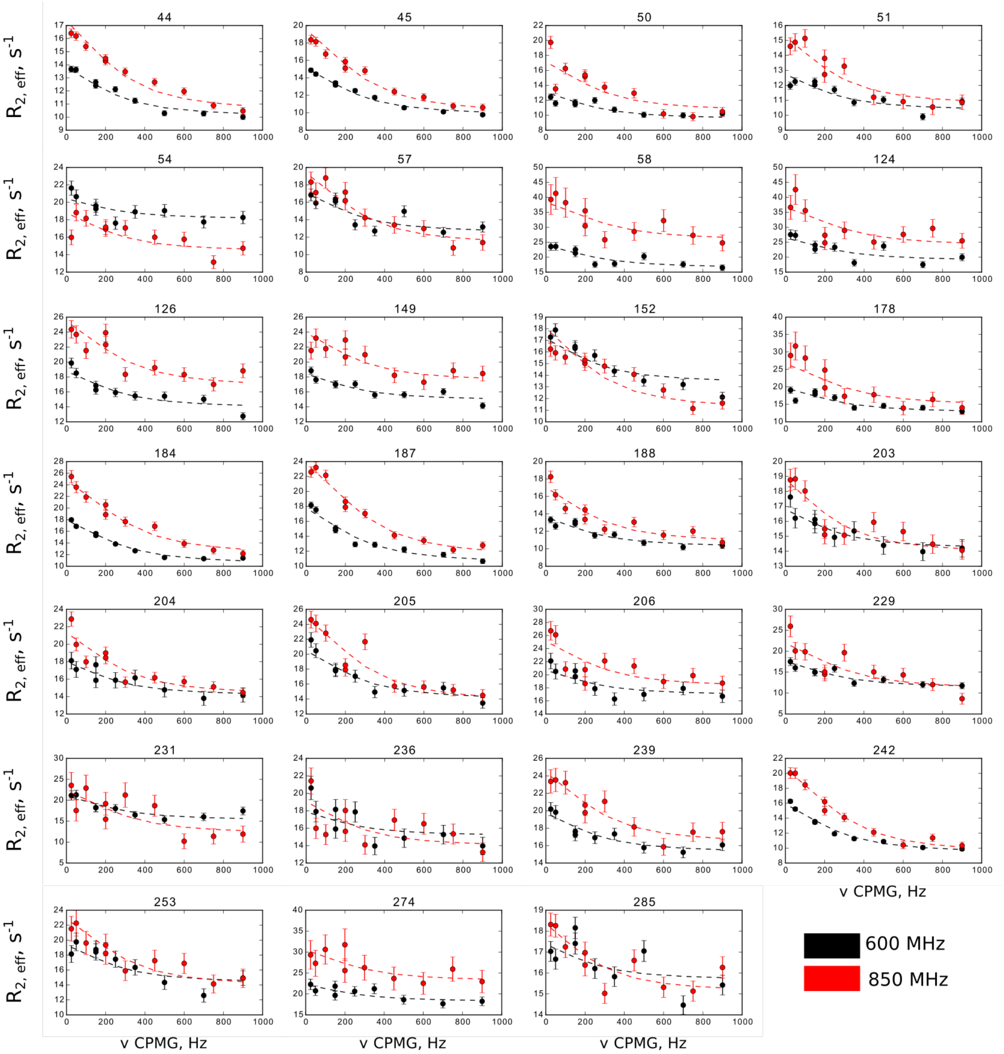

Figure S11: Comparison of non-flat ^{15}N CPMG relaxation dispersion profiles of apo GGC1 (black) and GGC1 in the presence of 6 mM cardiolipin (red) recorded at a ^{1}H Larmor frequency of 700 MHz. Numbers above each panel indicated residue number of GGC1. To facilitate the comparison of the CPMG dispersion curves, an additive offset of $R_{2,\mathrm{eff}}$ was added to some residues. Such an offset does not have any impact on the fit results, because the plateau is not attributed any physical meaning in terms of exchange. All fit parameters are reported in Table S1.

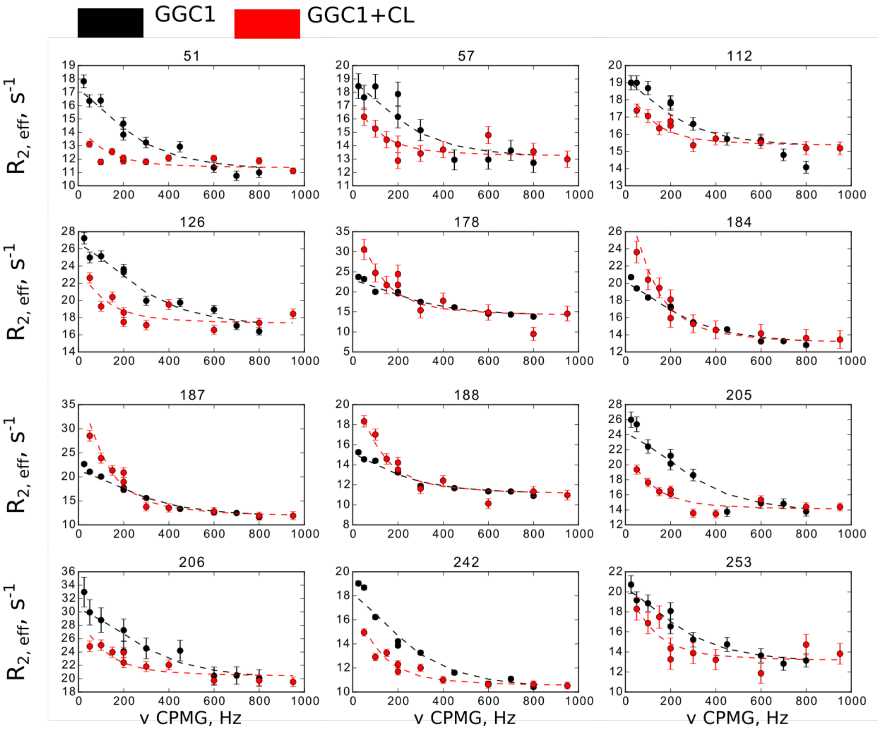

Figure S12: ^{15}N CPMG RD profiles of GGC1$^{2P\rightarrow 2R}$. All fit parameters are reported in Table S1. Figure is continued as Figure S13

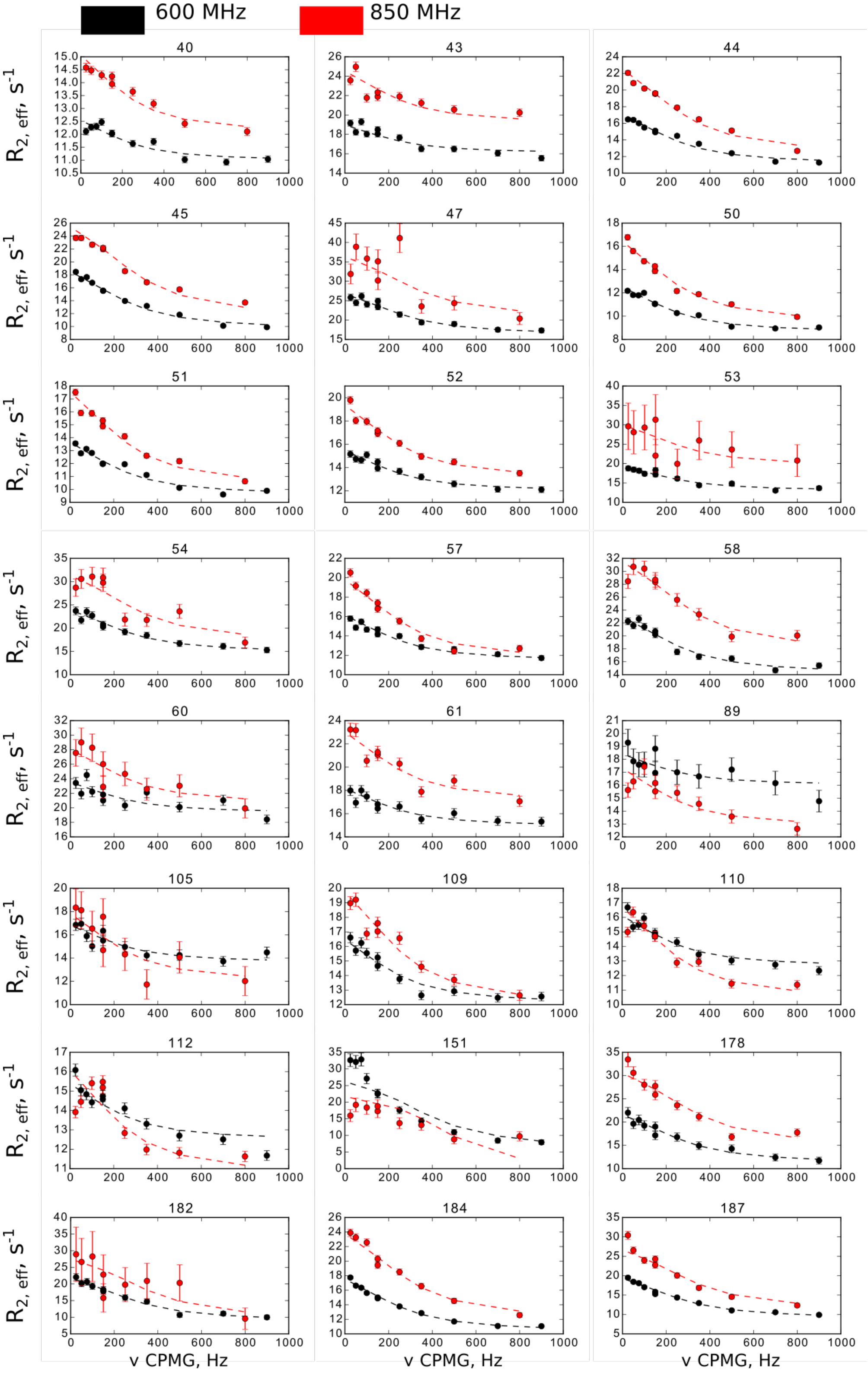

Figure S13: ^{15}N CPMG RD profiles of GGC1$^{2P \rightarrow 2R}$. Figure continued from Figure S12

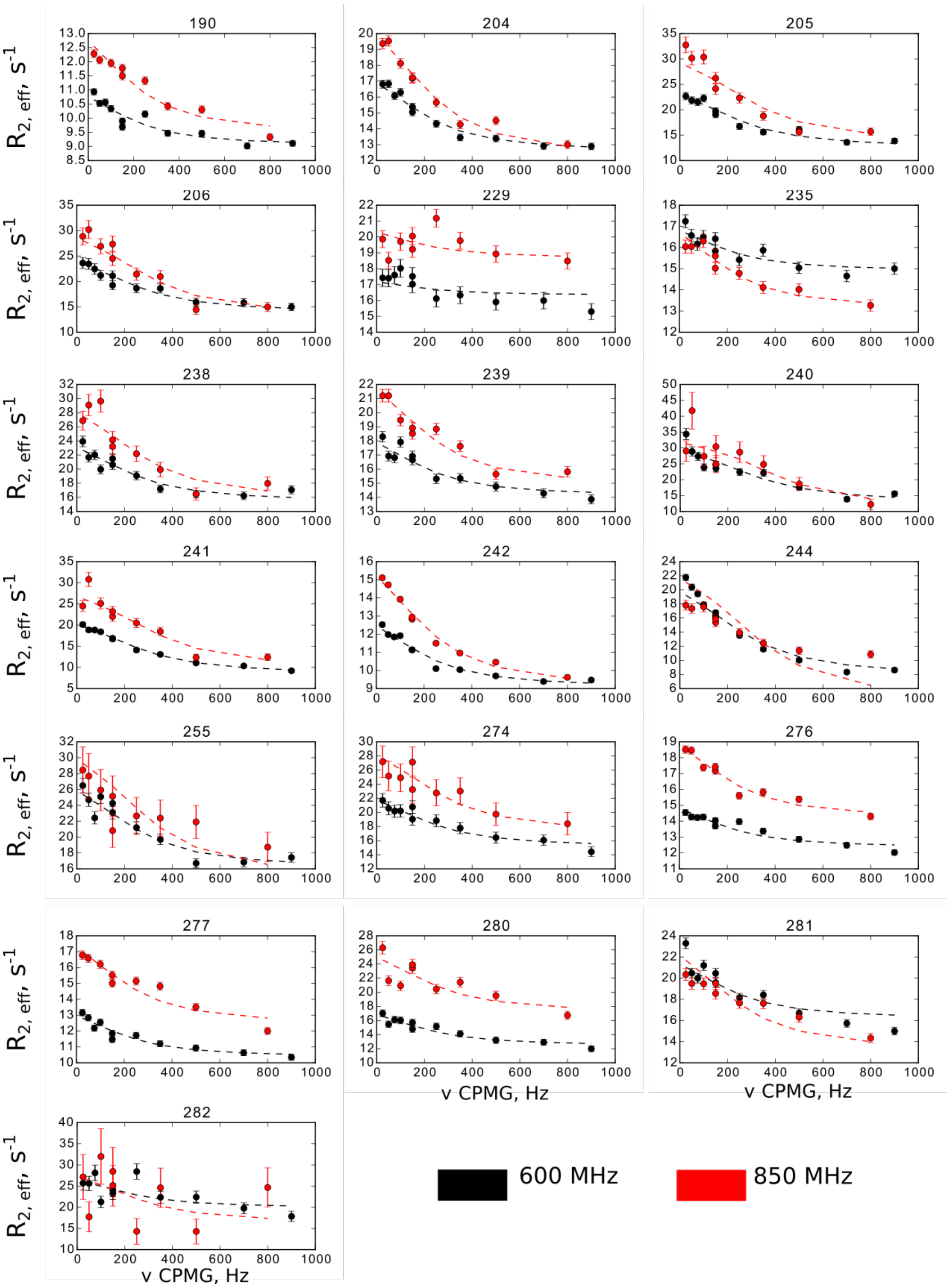

Figure S14: ^{15}N CPMG RD profiles of AAC3 and AAC3$^{\ominus\text{c-saltbridge}}$ mutant. (A) Data as reported earlier by Brüschweiler *et al*,[4] along with a fit to these data, performed as part of this study using the program ChemEx. (B) Data of AAC3$^{\ominus\text{c-saltbridge}}$ along with curves showing a fit of a two-state model. All fit parameters are reported in Table S1.

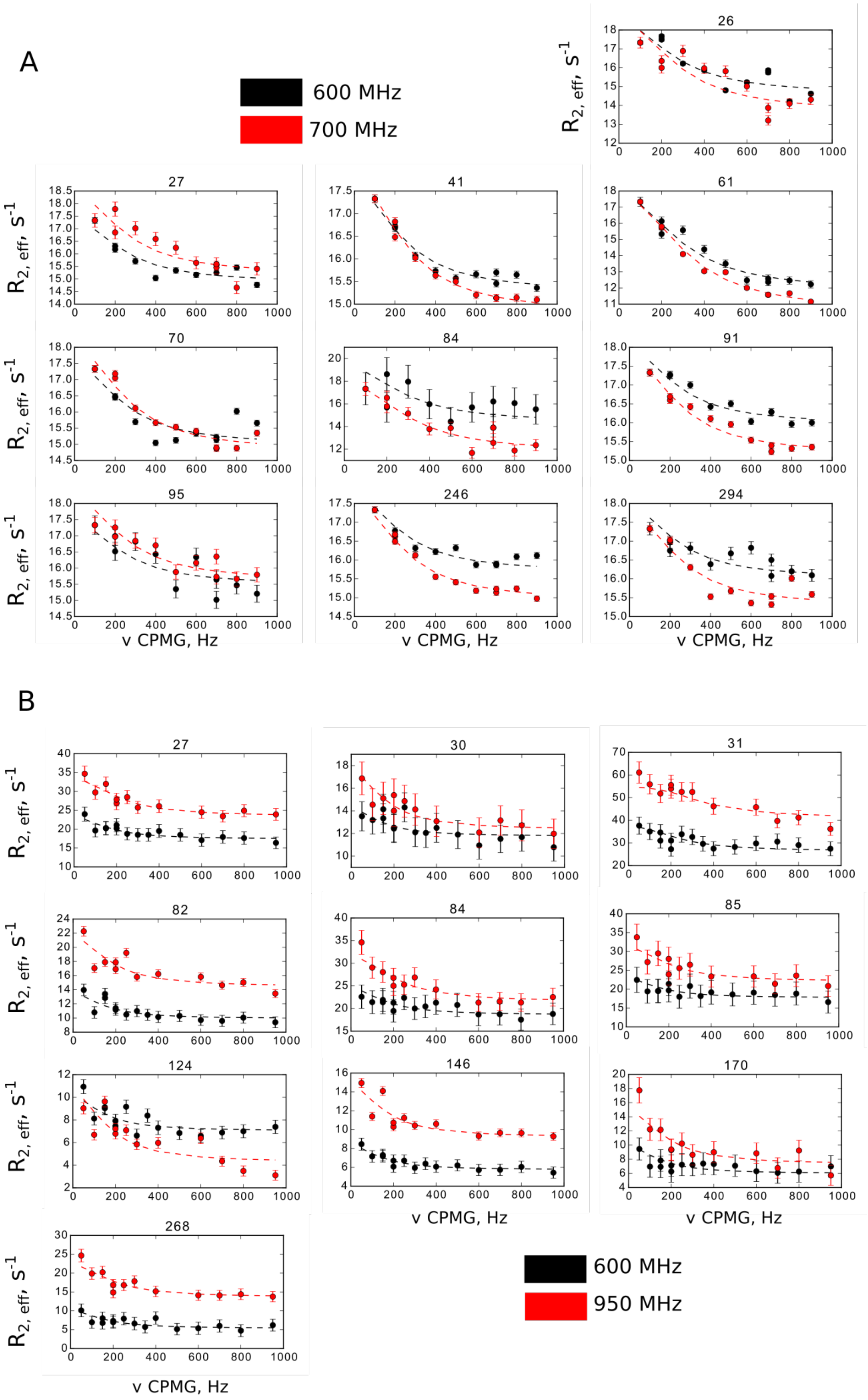

Figure S15: ^{15}N CPMG RD profiles of GGC1 in the presence of cardiolipin, compared to those of GGC1 in the presence of cardiolipin and GTP. All fit parameters are reported in Table S1.

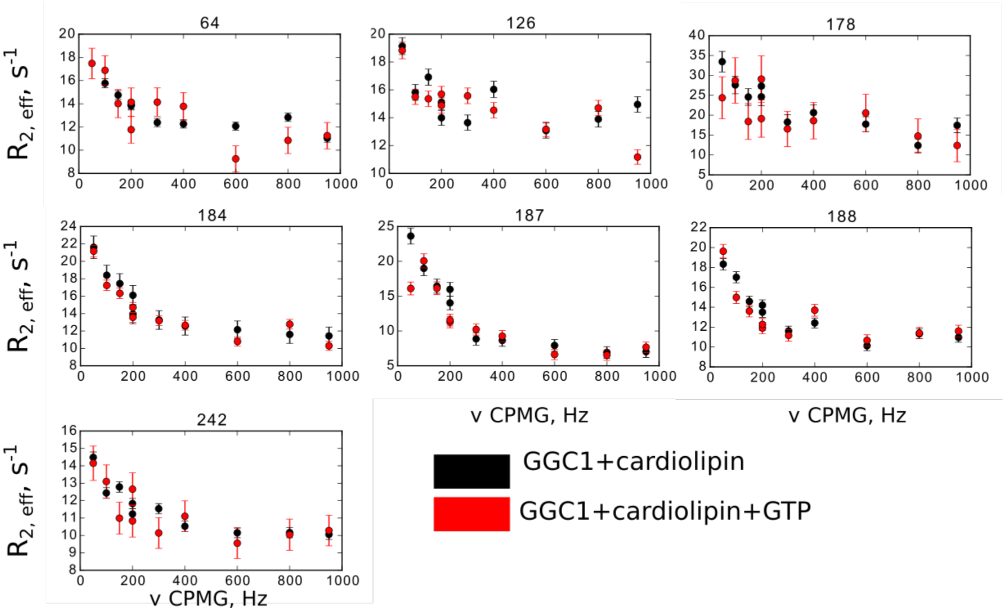

Figure S16: ^{15}N CPMG RD profiles of ORC1 at two different magnetic field strengths (600, 850 MHz ^{1}H Larmor frequency). The dashed lines show a global fit to a two-state model. All fit parameters are reported in Table S1.

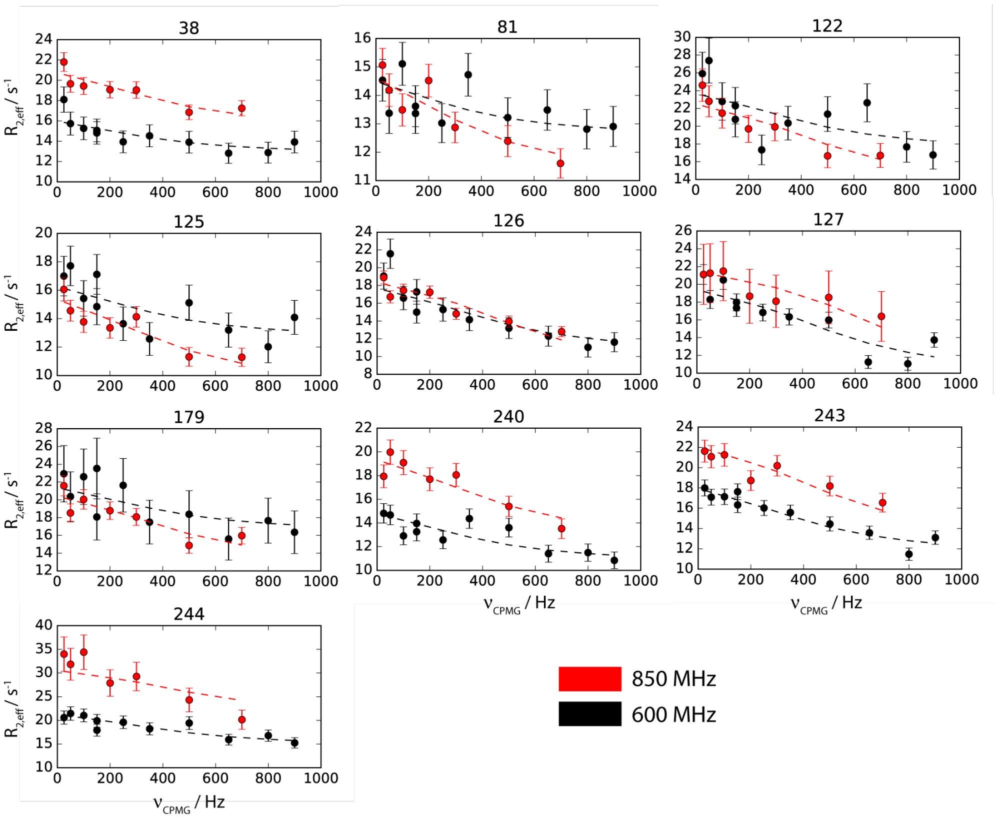

Figure S17: Comparison of non-flat ^{15}N CPMG relaxation dispersion profiles of wild-type GGC1 (black) and GGC1$^{2P\rightarrow 2R}$ (red) in the presence of 6 mM cardiolipin recorded on a 850 MHz spectrometer. Numbers above each panel indicated the residue number of GGC1. The dispersion profiles are nearly identical, indicating very similar millisecond dynamics experienced by the corresponding residues. Residue 51 is located in the mitochondrial helix. To facilitate the comparison of the CPMG dispersion curves, an additive offset of $R_{2,\mathrm{eff}}$ (i.e. plateau $R_{2,\mathrm{eff}}$) was added to some residues. Such an offset does not have any impact on the fit results, because the plateau is not attributed any physical meaning in terms of exchange. All fit parameters are reported in Table S1.

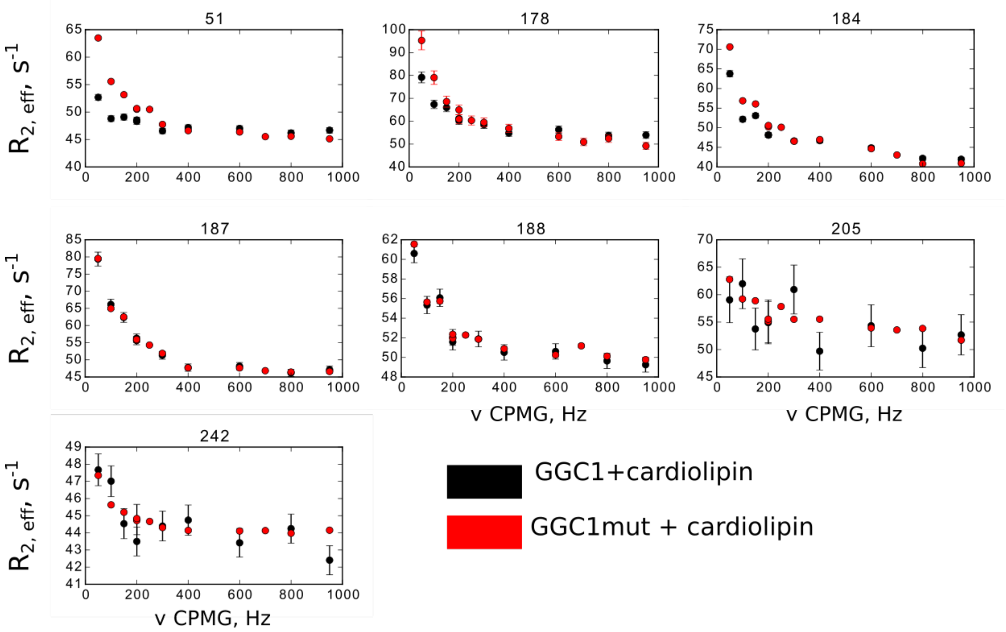

Figure S18: Results of ^{15}N CPMG RD fitting by jackknife analysis of three different GGC1 samples. (A) apo wild-type GGC1. (B) wild-type GGC1 in the presence of 20 mM GTP. (C) GGC1$^{2P\rightarrow 2R}$ mutant. In each panel the fitted exchange rate constant and minor-state population are shown for 200 different fits. In each fit the data of 60% of the residues, out of a total pool of 20 residues displaying exchange, were used, and jointly fitted to a two-state exchange model. The populations of the minor state and exchange rates are almost independent of the sub-cluster of residues used in the fit, suggesting that a global exchange model describes the data well. The data points are color-coded with respect to the chi-square value of the fit.

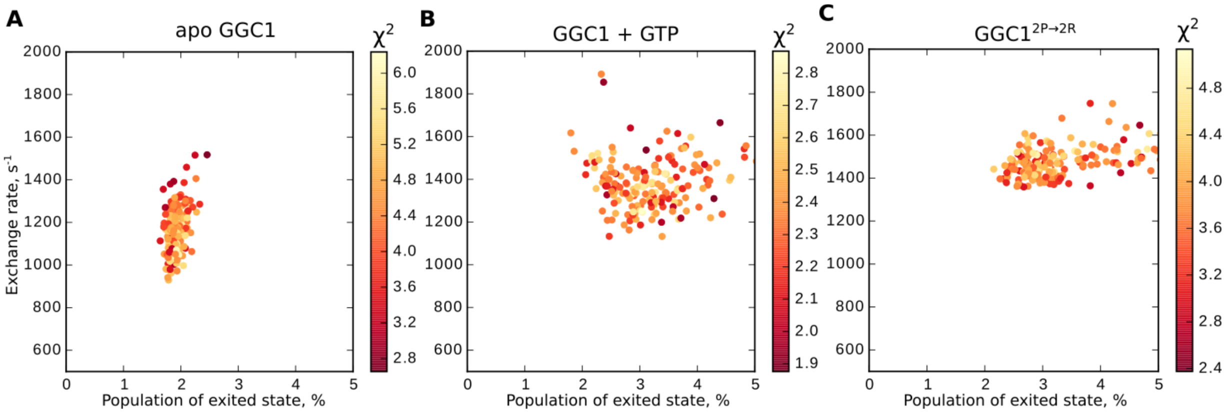

Figure S19: Chemical-shift perturbations (CSPs) upon introducing multiple mutations into GGC1 or AAC3. (A,B) CSPs in GGC1 upon introducing two proline-to-arginine substitutions (Pro138Arg, Pro230Arg), thereby creating GGC1$^{2P\rightarrow 2R}$, plotted onto a structural model of GGC1 (A). Spheres indicates the amide sites for which CSP data were available. Colors correspond to the combined chemical shift perturbations in 3D BT-HNCO spectra, scaled by the relative gyromagnetic ratios, and are related to the color-bar above. The substituted residues are indicated as red balls. (B) Overlay of wild-type GGC1 (red) and GGC1$^{2P\rightarrow 2R}$ spectra (black). The signals denote with an orange asterisk (around 115 ppm in the red and 120 ppm in the black spectrum) correspond to side-chain sites (presumably Arg), and are spectrally aliased, they resonate outside the chosen spectral widths, which were set differently in the two experiments. This apparent difference of spectra is, therefore, not an actual difference of resonance frequencies, but due to the acquisition setting. (C-E) CSPs resulting from the five mutations (as indicated in (C)), present in the AAC3$^{\circleddash\text{c-saltbridge}}$ construct relative to a previously used construct.[4] In addition to the three mutations of the cytosolic salt bridge network (K101D, K204D, Q298D), positions 233 and 277 are cysteines in the wild-type yeast AAC3, and were replaced by different residue types in the NMR studies (Val/Ala in reference[4] and Ala/Ser in this study). Panel (C) plots magnitude of the CSPs in HNCO spectra, as calculated according to equation 1, onto the amide sites in the X-ray structure of AAC3 (PDB ID 4C9Q). The differences were obtained by comparing chemical shifts determined in this study (AAC3$^{\circleddash\text{c-saltbridge}}$) with those reported in BMRB entry 26589. Red spheres indicate the mutation sites, while the residues without spheres correspond to the residues for which assignment could not be transferred. (D) Chemical shift perturbations, as reported in panel (C), plotted as a function of the residue number. Gray and blue cylinders represent TM and matrix helices, respectively. Red lines indicate mutation sites and the corresponding substitutions. (E) For comparison, we plot the differences of chemical shifts of HNCO sites in GGC1, determined in this study and reported previously.[11] Even though the buffer compositions and pH values in the two studies were the same, small CSPs are detected along the sequence. This data shows that the magnitude of CSPs detected in the same protein in different laboratories (E) is similar to the one found for the AAC3 constructs with five differences in sequence, stressing that the CSPs in AAC3 are indeed very small. Horizontal dashed lines indicate 3 times the standard deviation over all residues.

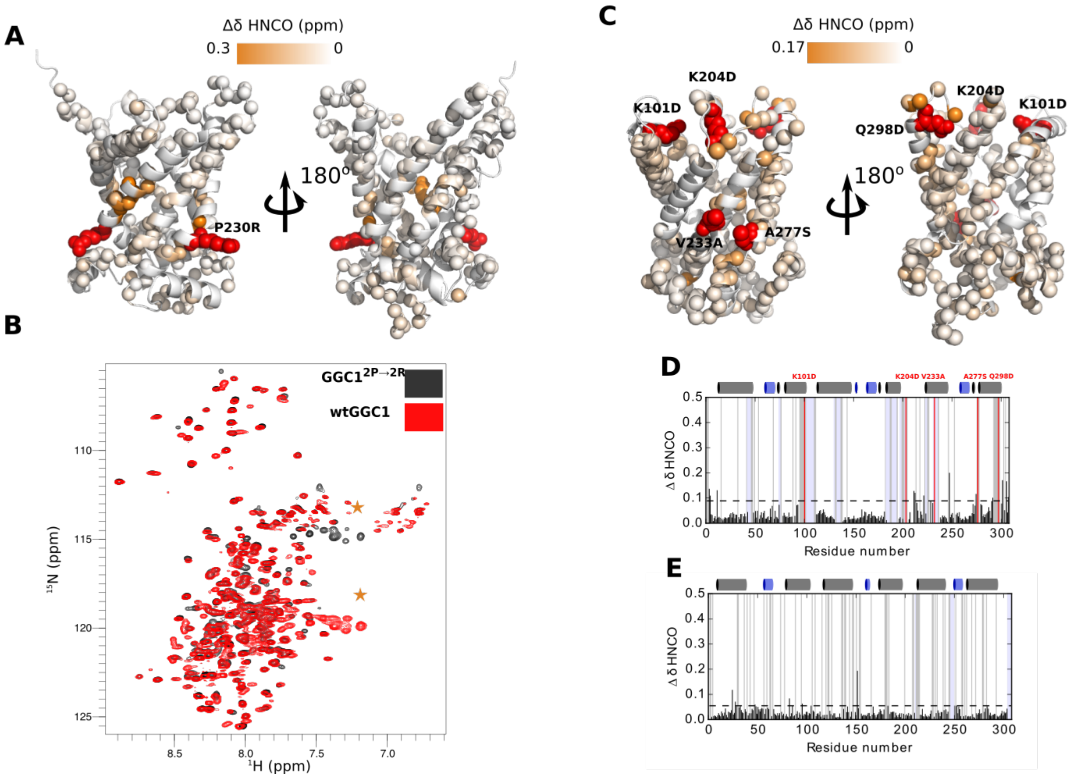

Figure S20: Spectral changes of GGC1 and GGC1$^{2P\rightarrow 2R}$ (GGC1 mutant) upon addition of cardiolipin or the chemically similar POPG. Shown are 2D spectra without/with CL or POPG of GGC1 (A,C,D) and GGC1$^{2P\rightarrow 2R}$ (B). Widespread chemical-shift perturbations indicate interaction of CL with GGC1 and its non-functional mutant. Comparison of panels (A) and (B) suggest that these changes are similar in both protein constructs, suggesting that the introduction of two Arg residues in TM helices does not alter the CL interaction in DPC micelles. When extracted from native membranes with a mild detergent, CL is tightly attached to MCs; CLs remain bound to AAC, for example, during long purification steps and could be detected in crystal structures.[23] In DPC micelles the addition of CL leads to [CL]-concentration-dependent shifts, rather than to the disappearance of peaks corresponding to a non-CL-bound state and appearance of a CL-bound state. The latter (so-called slow-exchange regime) behavior would be expected for a tight interaction. Although not a proof, we suspected that the CL interaction in DPC micelles may not be as specific and tight as in native protein. To provide further evidence for this hypothesis we performed an additional titration with POPG. CL is biosynthetically derived from the fusion of two POPG molecules, i.e. it bears twice the charge, and has four acyl chains instead of two. If the interaction is electrostatically driven, but not actually specific to CL, one would expect different behavior with CL and with POPG. The spectra in (C) and (D) suggest that this is not the case, as both lipids produce very similar chemical-shift changes on GGC1 in DPC.

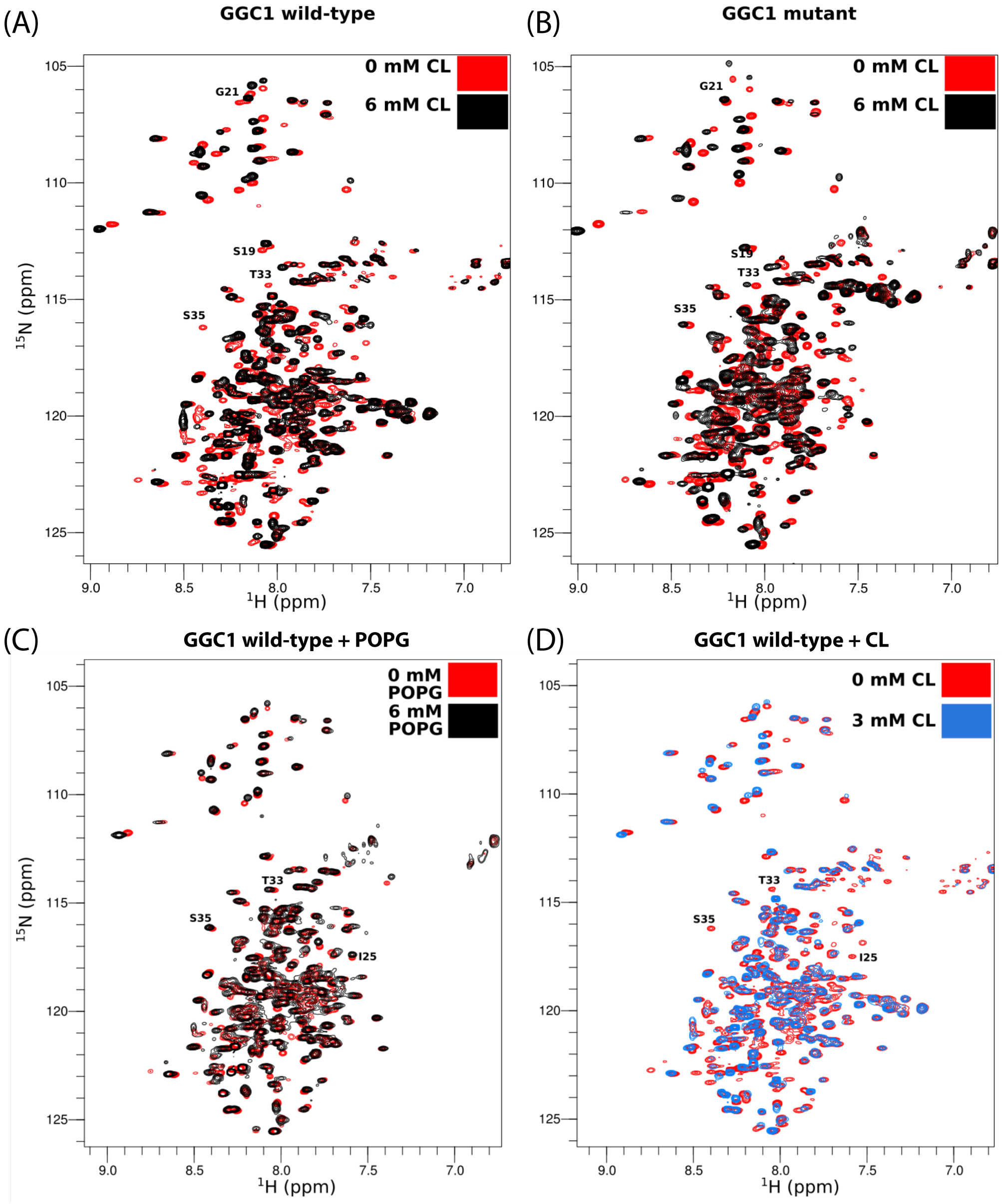

Figure S21: Interaction of AAC3 with ATP and GTP in DPC micelles. (A) 2D BEST-TROSY-HSQC spectra of AAC3$^{\ominus\text{c-saltbridge}}$ mutant binding to two different nucleotides. Left - overlay of apo AAC3$^{\ominus\text{c-saltbridge}}$ mutant spectrum (black) with the spectrum of AAC3$^{\ominus\text{c-saltbridge}}$ mutant in the presence of 20 mM of ATP (red). Right - overlay of AAC3$^{\ominus\text{c-saltbridge}}$ mutant spectra in the presence of either ATP (red) or GTP (blue). The residues displaying most pronounced chemical shift perturbations are indicated by stars. The lower two panels in (A) show a zoom into the glycine region of these spectra, as well as a zoom onto the cross-peak of Arg141. Brüschweiler *et al*[4] have recently reported ADP-induced CSPs of this residue in WT AAC3, which are of very similar amplitude as those found here in the AAC3$^{\ominus\text{c-saltbridge}}$ mutant. (B) shows CSPs induced by ATP (red) and GTP (black), plotted as a residue-wise combined (^{1}H, ^{15}N) CSPs obtained from 2D spectra. Gray and blue cylinders on top indicate the TM and matrix helices, respectively, as obtained from the crystal structure of AAC3. Although the data completeness is reduced by the fact that only 2D spectra were available, it appears that the largest chemical shift perturbations do not occur in the TM helix region but in loop regions or the interfacial helices. (C) plots the same data as in B, displayed as a correlation of ATP and GTP induced chemical shift perturbations. (D) Electrostatic surface representation of AAC3 (PDB entry 4C9Q), viewed into the central cavity (units K_BT/e_c).

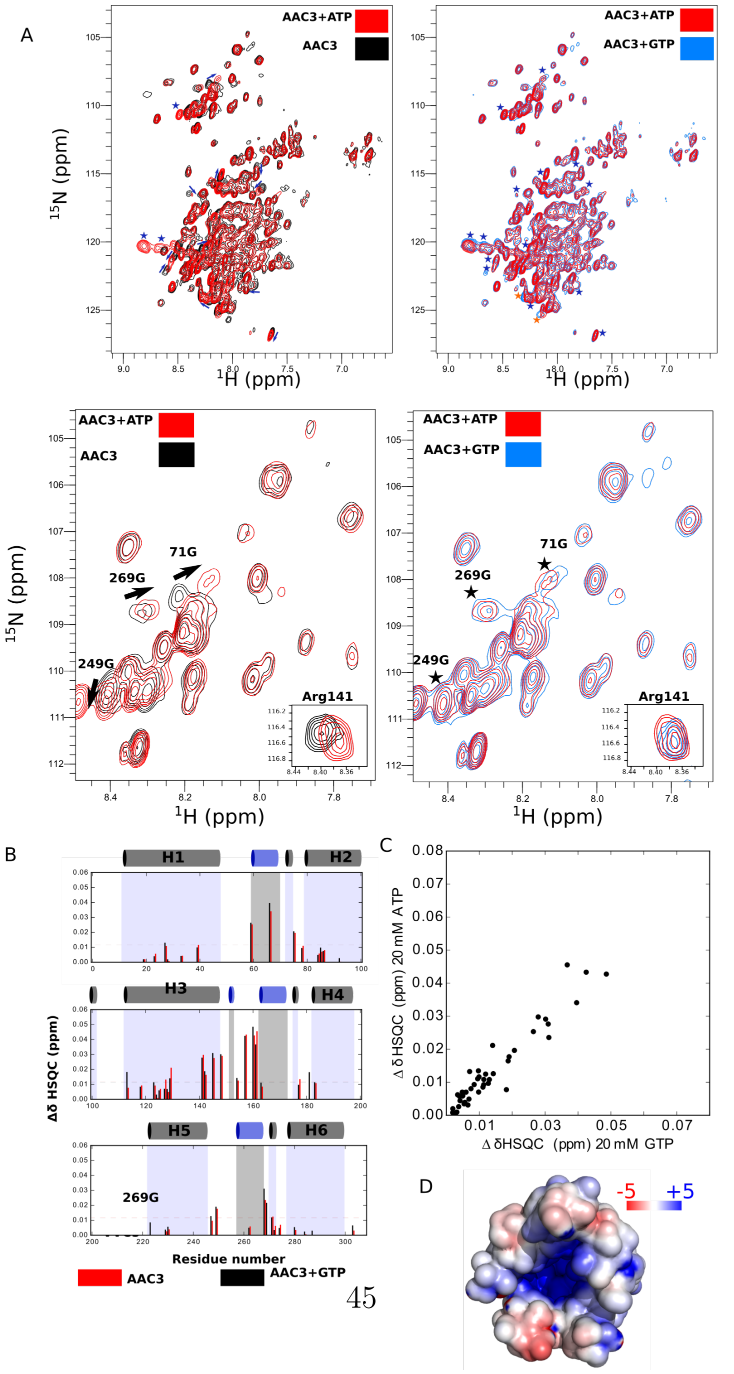

Figure S22: Comparison of chemical shift perturbations upon addition of 20 mM GTP for wild- type GGC1 (red bars) and GGC12P2R (black bars). A, residue-wise chemical shift perturbations in the three dimensions (see equation 1) against residue numbers in wild-type GGC1 and GGC1$^{2P\rightarrow 2R}$. Light blue shaded background indicated regions where chemical shift perturbations are not known for wild-type GGC1. Grey shaded background indicated missing information about the chemical shift perturbations for GGC1$^{2P\rightarrow 2R}$. Red shaded regions indicate the position of mutations (Pro138Arg and Pro230Arg). Gray and blue cylinders above indicate TM and matrix helices as determined from the homology model of GGC1. B, the same data as in A plotted in a different way to represent the correlation between the wild-type GGC1 and GGC1$^{2P\rightarrow 2R}$ for GTP binding.

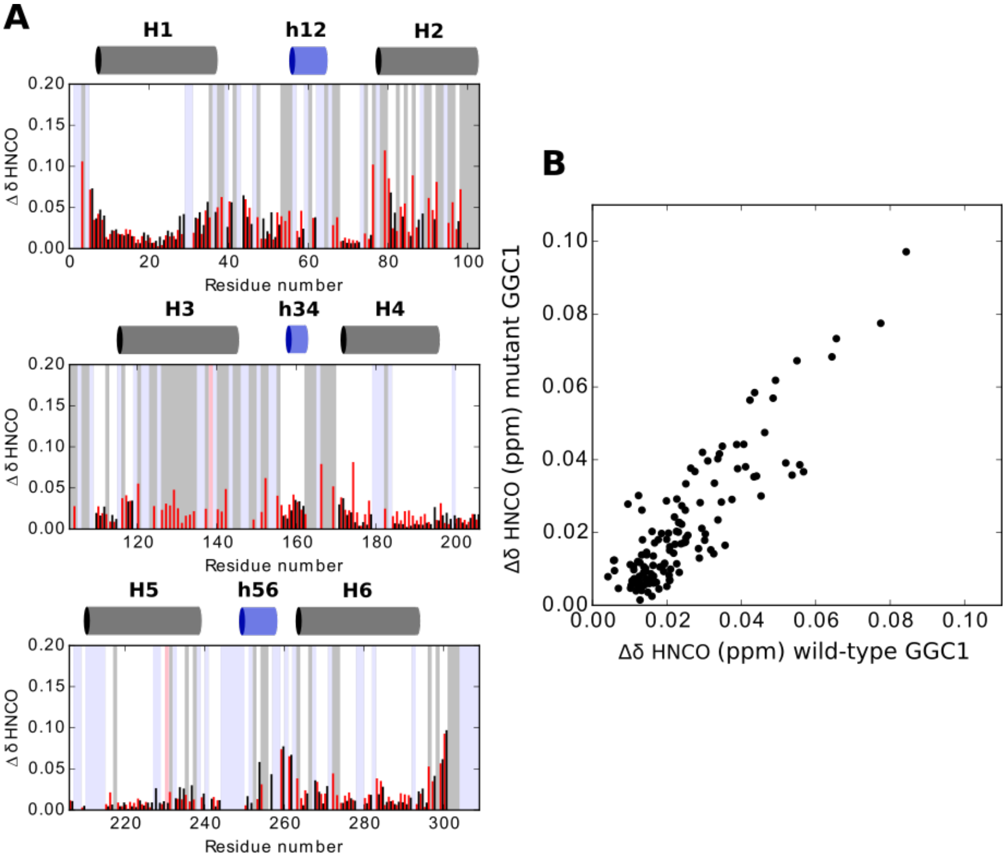

Figure S23: Binding of CATR to GGC1 (a-c) and AAC3 (d-f). (a,d). 2D HN correlation spectra of GGC1 (a) and AAC3 (d) at different concentrations of CATR. A zoom onto an example of a residue with large CSPs is shown indicated by a box. (b,e) Residue-wise CSPs (calculated from absolute changes of ^{1}H and ^{15}N shift, normalized by the respective gyromagnetic ratios), extracted from these spectra at a concentration of 5 (b) and 7.5 (e) mM, respectively. (c,f) The CSPs shown in panels (b,e) are plotted onto the structure with a color scale from white (no CSP) to red/blue (largest observed CSP). As shown by these data, the CATR interaction concerns residues spread over the entire molecule in both GGC1 and AAC3, not only residues in the central cavity. The fact that the CSPs observed in AAC3, which is supposed to bind CATR, are similar to those in GGC1, which is not supposed to bind CATR, suggests that these interactions are physiologically relevant. The data shown in panels (d-f) were kindly provided by S. Brüschweiler, and published in reference[4]).

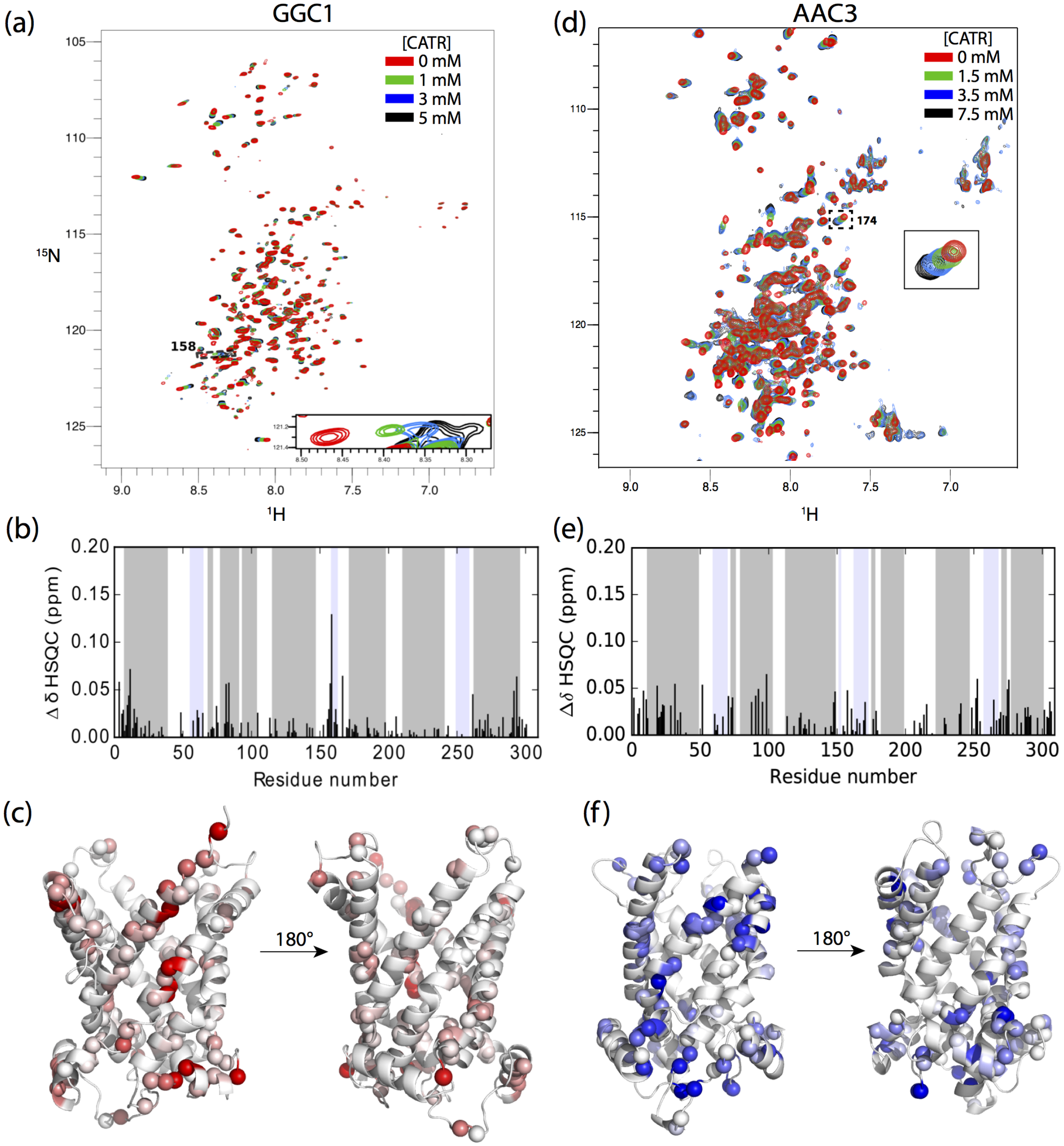

Figure S24: Chemical-shift perturbations observed in ORC1 upon addition of 90 mM L-histidine (A) or 80 mM NaCl (B). Top: residue-wise chemical shift perturbations extracted from the HNCO spectra below. Horizontal dashed line represents 3 standard deviations extracted by analysing all chemical shift perturbations for assigned residues. The scale of the ordinate in the bar-plot is kept the same as in the previous examples for GGC1 binding, to allow easier visual comparison of the binding data for the two proteins. Bottom: project along the ^{1}H dimension of BEST-TROSY-HNCO spectra in the presence and absence of aforementioned solutes. Inserts show residues which show perturbations in the presence of charged solutes that correspond to the largest bars in the upper plots. The decrease of signal intensity after addition of NaCl might be attributed to the decreased sensitivity of cryogenic probe at higher salt concentrations. (C) shows the electrostatic surface potential of a structural model of ORC1, with the same scale as the ones shown in Figure 3D and S21D (units K_BT/e_c). Note that ORC1 has significantly less charges than AAC3 and GGC1, and its substrates are less charged than ATP/GTP/CATR, possibly providing an explanation why (non-specific) interactions are formed to a smaller extent as in AAC3 and GGC1.

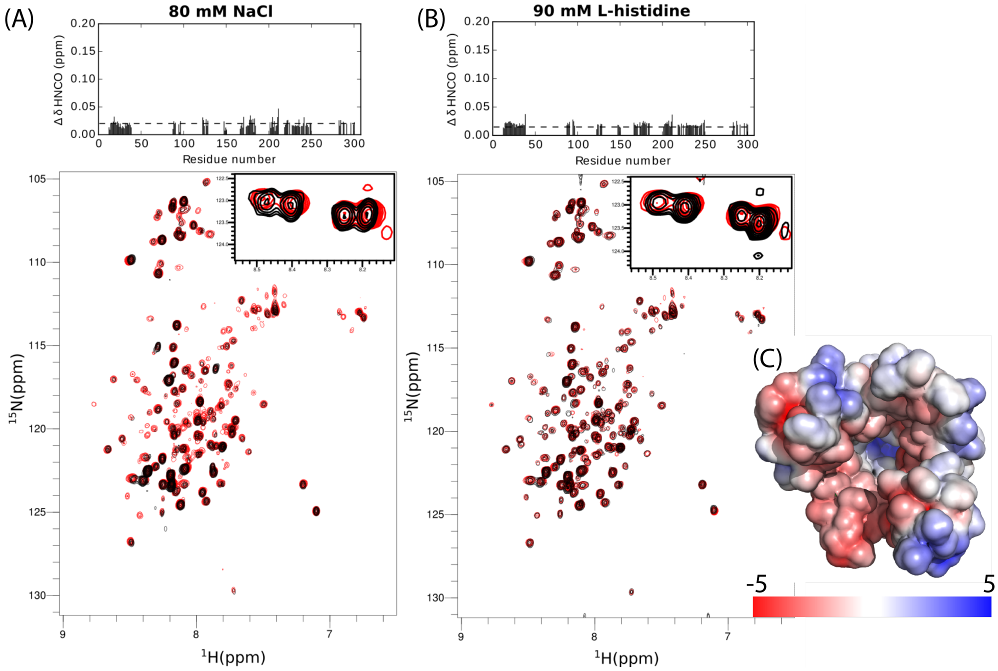

Figure S25: Time evolution of the root-mean-square displacement (RMSD) of bAAC3 backbone atomic positions with respect to those in the crystal structure. Only the evolution during the last 500 ns of the trajectory is plotted.

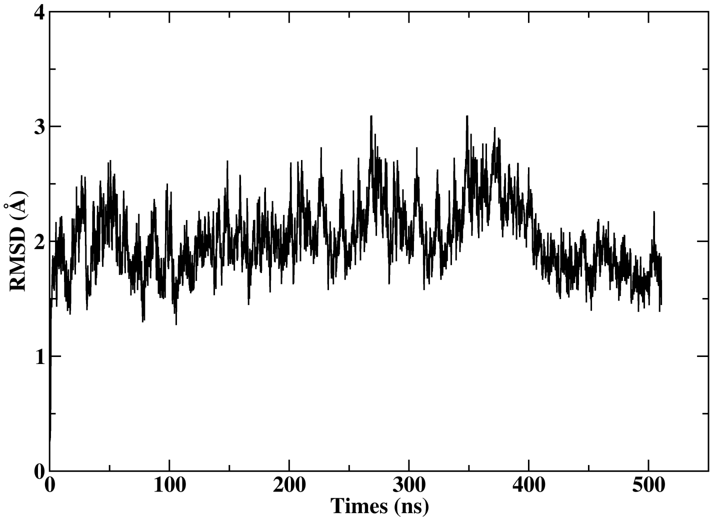

Figure S26: (Left) Top and (right) bottom views of bovine AAC (ice blue) embedded in a DPC micelle (tails: yellow surfaces, head groups: purple spheres) obtained from MD simulations.

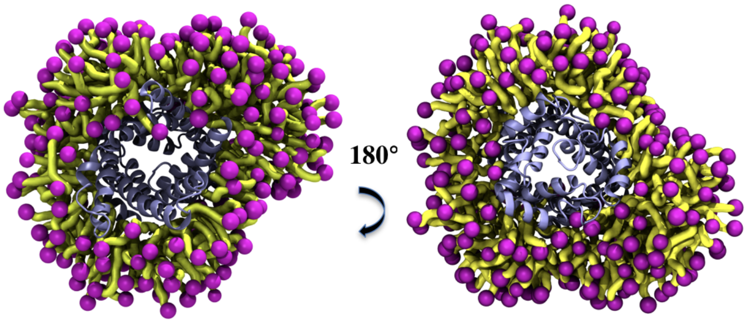

Figure S27: (Left) Side and (right) top views of yAAC3 obtained from MD simulations. (A), (B) and (C) represent the secondary structures of the protein before and after applying the TALOS+ restraints and at the end of the trajectory, respectively. Purple: α-helix, cyan: turn, white: coil, blue: 3_{10}-helix.

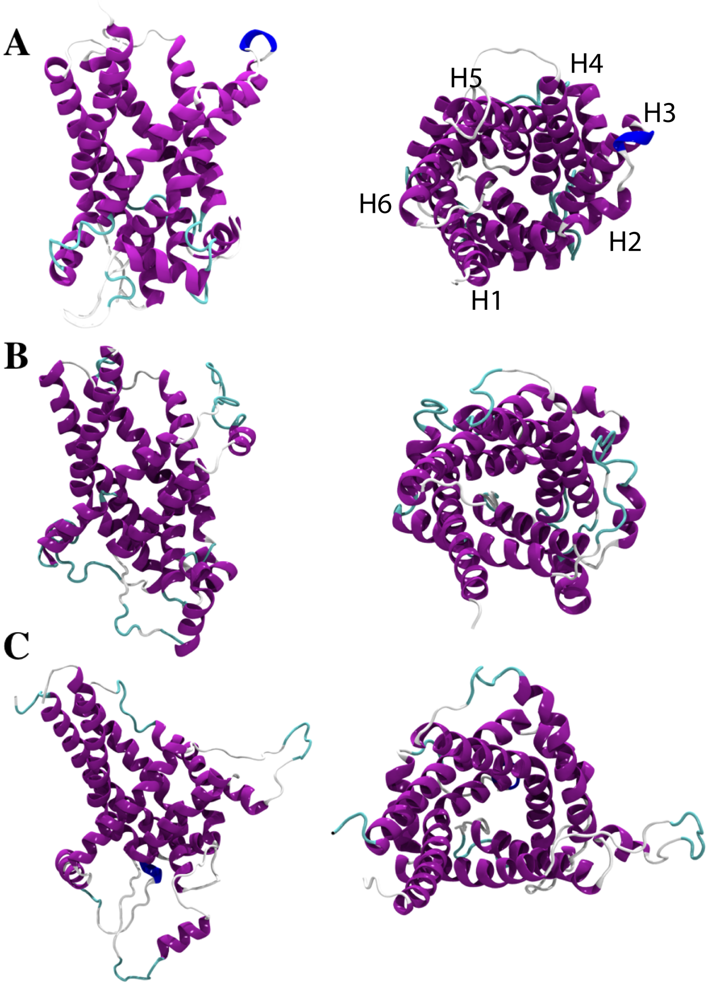

Figure S28: The use of different detergents for determining membrane protein structures. These statistics have been obtained from analyses of structures deposited in the PDB, with the aid of data bases (http://blanco.biomol.uci.edu/mpstruc/ and http://www.drorlist.com/nmr/MPNMR.html). Panels (A), (B) and (C) show the percentages of detergents used by crystallography, electron microscopy and solution-NMR, respectively. Panel (D) shows statistics of different types of MPs, solved by solution-NMR. Irrespective of the type of membrane protein, DPC has been by far the most widely used detergent in solution-NMR, but it has a rather modest track record for other structural techniques (crystallography, EM). Our data suggest that a plausible reason for this observed difference in detergent use may be the ability of DPC to keep MPs in solution in a highly dynamics state that is unable to crystallize. Alternatively, the detergent itself may interfere with the crystallization process.

(a) Membrane mimetics for crystal structures

(b) Membrane mimetics for EM structures

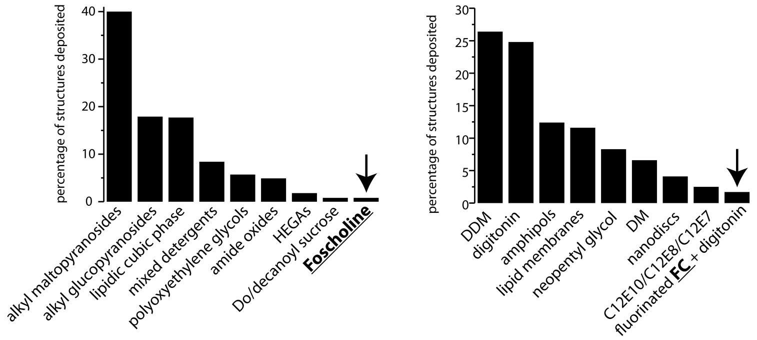

(c) Membrane mimetics for solution-NMR structures

(d) Foscholine in solution-NMR

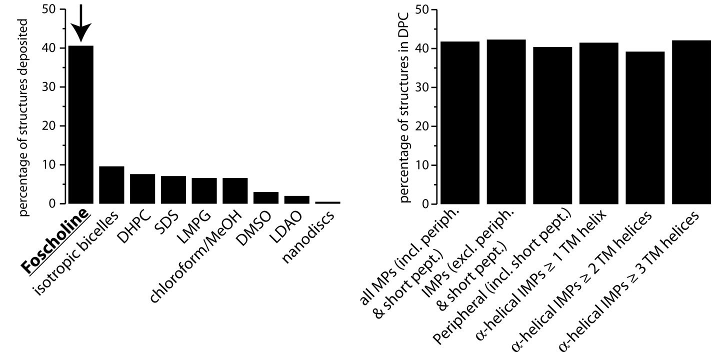

Movie M1: 1.1 µs molecular-dynamics simulation of yeast AAC3 in DPC. After 100 ns TALOS+ restraints are applied for 100 ns. From 200 ns to the end of the simulation the protein evolves freely in DPC.

Movie M2: Same as movie M1 including the explicit representation of DPC organization around yAAC3. (Tails: yellow surfaces, head groups: purple spheres).

References

(1) Kunji, E. R.; Aleksandrova, A.; King, M. S.; Majd, H.; Ashton, V. L.; Cerson, E.; Springett, R.; Kibalchenko, M.; Tavoulari, S.; Crichton, P. G.; Ruprecht, J. J. The transport mechanism of the mitochondrial ADP/ATP carrier. *Biochim. Biophys. Acta* **2016**, *1863*, 2379–2393.

(2) Claypool, S. M. Cardiolipin, a critical determinant of mitochondrial carrier protein assembly and function. *Biochim. Biophys. Acta* **2009**, *1788*, 2059–68.

(3) Monne, M.; Miniero, D. V.; Daddabbo, L.; Palmieri, L.; Porcelli, V.; Palmieri, F. Mitochondrial transporters for ornithine and related amino acids: A review. *Amino Acids* **2015**, *47*, 1763–1777.

(4) Brüschweiler, S.; Yang, Q.; Run, C.; Chou, J. J. Substrate-modulated ADP/ATP-transporter dynamics revealed by NMR relaxation dispersion. *Nat. Struct. Mol. Biol.* **2015**, *22*, 636–641.

(5) Bamber, L.; Bamber, L.; Harding, M.; Harding, M.; Butler, P. J. G.; Butler, P. J. G.; Kunji, E. R. S.; Kunji, E. R. S. Yeast mitochondrial ADP/ATP carriers are monomeric in detergents. *Proc. Natl. Acad. Sci. U.S.A.* **2006**, *103*, 16224–16229.

(6) Hashimoto, M.; Majima, E.; Goto, S.; Shinohara, Y.; Terada, H. Fluctuation of the first loop facing the matrix of the mitochondrial ADP/ATP carrier deduced from intermolecular cross-linking of Cys56 residues by bifunctional dimaleimides. *Biochemistry* **1999**, *38*, 1050–1056.

(7) Kunji, E. R. S.; Harding, M. Projection structure of the atractyloside-inhibited mitochondrial ADP/ATP carrier of Saccharomyces cerevisiae. *J. Biol. Chem.* **2003**, *278*, 36985–36988.

(8) King, M. S.; Kerr, M.; Crichton, P. G.; Springett, R.; Kunji, E. R. Formation of a cytoplasmic salt bridge network in the matrix state is a fundamental step in the transport mechanism of the mitochondrial ADP/ATP carrier. *Biochim Biophys Acta* **2016**, *1857*, 14–22.

(9) Alexandrov, A. I.; Mileni, M.; Chien, E. Y. T.; Hanson, M. A.; Stevens, R. C. Microscale Fluorescent Thermal Stability Assay for Membrane Proteins. *Structure* **2008**, *16*, 351–359.

(10) Crichton, P. G.; Lee, Y.; Ruprecht, J. J.; Cerson, E.; Thangaratnarajah, C.; King, M. S.; Kunji, E. R. S. Trends in thermostability provide information on the nature of substrate, inhibitor, and lipid interactions with mitochondrial carriers. *J. Biol. Chem.* **2015**, *290*, 8206–17.

(11) Sounier, R.; Bellot, G.; Chou, J. J. Mapping conformational heterogeneity of mitochondrial nucleotide transporter in uninhibited States. *Angew Chem Int. Ed.* **2015**, *54*, 2436–41.

(12) Lunetti, P.; Cappello, A. R.; Marsano, R. M.; Pierri, C. L.; Carrisi, C.; Martello, E.; Caggese, C.; Dolce, V.; Capobianco, L. Mitochondrial glutamate carriers from Drosophila melanogaster: Biochemical, evolutionary and modeling studies. *Biochim. Biophys. Acta* **2013**, *1827*, 1245–1255.

(13) Iacopetta, D.; Madeo, M.; Tasco, G.; Carrisi, C.; Curcio, R.; Martello, E.; Casadio, R.; Capobianco, L.; Dolce, V. A novel subfamily of mitochondrial dicarboxylate carriers from Drosophila melanogaster: Biochemical and computational studies. *Biochim. Biophys. Acta* **2011**, *1807*, 251–261.

(14) Madeo, M.; Carrisi, C.; Iacopetta, D.; Capobianco, L.; Cappello, A. R.; Bucci, C.; Palmieri, F.; Mazzeo, G.; Montalto, A.; Dolce, V. Abundant expression and purification of biologically active mitochondrial citrate carrier in baculovirus-infected insect cells. *J. Bioenerg.* **2009**, *41*, 289–297.

(15) Orekhov, V. Y.; Jaravine, V. A. Analysis of non-uniformly sampled spectra with multi-dimensional decomposition. *Prog. Nucl. Magn. Reson. Spectr.* **2011**, *59*, 271–292.

(16) Delaglio, F.; Grzesiek, S.; Vuister, G.; Zhu, G.; Pfeifer, J.; Bax, A. NMRPIPE - a multidimensional spectral processing system based on Unix pipes. *J. Biomol. NMR* **1995**, *6*, 277–293.

(17) Vranken, W. F.; Boucher, W.; Stevens, T. J.; Fogh, R. H.; Pajon, A.; Llinas, M.; Ulrich, E. L.; Markley, J. L.; Ionides, J.; Laue, E. D. The CCPN data model for NMR spectroscopy: development of a software pipeline. *Proteins* **2005**, *59*, 687–96.

(18) Sounier, R.; Mas, C.; Steyaert, J.; Laeremans, T.; Manglik, A.; Huang, W.; Kobilka, B. K.; Déméné, H.; Granier, S. Propagation of conformational changes during m-opioid receptor activation. *Nature* **2015**, *524*, 375–9.

(19) Favier, A.; Brutscher, B. Recovering lost magnetization: polarization enhancement in biomolecular NMR. *J. Biomol. NMR* **2011**, *49*, 9–15.

(20) Franco, R.; Gil-Caballero, S.; Ayala, I.; Favier, A.; Brutscher, B. Probing Conformational Exchange Dynamics in a Short-Lived Protein Folding Intermediate by Real-Time Relaxation–Dispersion NMR. *J. Am. Chem. Soc.* **2017**, *139*, 1065–1068.

(21) Korzhnev, D. M.; Kloiber, K.; Kanelis, V.; Tugarinov, V.; Kay, L. E. Probing slow dynamics in high molecular weight proteins by methyl-TROSY NMR spectroscopy: application to a 723-residue enzyme. *J. Am. Chem. Soc.* **2004**, *126*, 3964–3973.

(22) Sekhar, A.; Rosenzweig, R.; Bouvignies, G.; Kay, L. E. Mapping the conformation of a client protein through the Hsp70 functional cycle. *Proc. Natl. Acad. Sci. U.S.A.* **2015**, *112*, 10395–10400.

(23) Ruprecht, J. J.; Hellawell, A. M.; Harding, M.; Crichton, P. G.; McCoy, A. J.; Kunji, E. R. S. Structures of yeast mitochondrial ADP/ATP carriers support a domain-based alternating-access transport mechanism. *Proc. Natl. Acad. Sci. USA* **2014**, *111*, E426–34.

(24) Pebay-Peyroula, E.; Dahout-Gonzalez, C.; Kahn, R.; Trezeguet, V.; Lauquin, G.; Brandolin, R. Structure of mitochondrial ADP/ATP carrier in complex with carboxyatractyloside. *Nature* **2003**, *426*, 39–44.

(25) Šali, A.; Blundell, T. L. Comparative Protein Modelling by Satisfaction of Spatial Restraints. *J. Mol. Biol.* **1993**, *234*, 779—815.

(26) Zoonens, M.; Comer, J.; Masscheleyn, S.; Pebay-Peyroula, E.; Chipot, C.; Miroux, B.; Dehez, F. Dangerous Liaisons between Detergents and Membrane Proteins. The Case of Mitochondrial Uncoupling Protein 2. *J. Am. Chem. Soc.* **2013**, *135*, 15174–15182.

(27) Martínez, L.; Andrade, R.; Birgin, E. G.; Martínez, J. M. PACKMOL: a package for building initial configurations for molecular dynamics simulations. *J. Comput. Chem.* **2009**, *30*, 2157–2164.

(28) Phillips, J. C.; Braun, R.; Wang, W.; Gumbart, J.; Tajkhorshid, E.; Villa, E.; Chipot, C.; Skeel, R. D.; Kale, L.; Schulten, K. Scalable molecular dynamics with NAMD. *J. Comput. Chem.* **2005**, *26*, 1781–1802.

(29) Humphrey, W.; Dalke, A.; Schulten, K. VMD: visual molecular dynamics. *J. Mol. Graph.* **1996**, *14*, 33–38.

(30) Feller, S. E.; Zhang, Y.; Pastor, R. W.; Brooks, B. R. Constant pressure molecular dynamics simulation: the Langevin piston method. *J. Chem. Phys.* **1995**, *103*, 4613–4621.

(31) Martyna, G. J.; Tobias, D. J.; Klein, M. L. Constant pressure molecular dynamics algorithms. *J. Chem. Phys.* **1994**, *101*, 4177–4189.

(32) Darden, T.; York, D.; Pedersen, L. Particle mesh Ewald: An N log (N) method for Ewald sums in large systems. *J. Chem. Phys.* **1993**, *98*, 10089–10092.

(33) Andersen, H. C. Rattle: A "velocity" version of the shake algorithm for molecular dynamics calculations. *J. Comput. Phys.* **1983**, *52*, 24–34.

(34) Tuckerman, M.; Berne, B. J.; Martyna, G. J. Reversible multiple time scale molecular dynamics. *J. Chem. Phys.* **1992**, *97*, 1990–2001.

(35) others,, et al. All-atom empirical potential for molecular modeling and dynamics studies of proteins. *J. Phys. Chem. B* **1998**, *102*, 3586–3616.

(36) MacKerell Jr, A. D.; Feig, M.; Brooks, C. L. Improved treatment of the protein backbone in empirical force fields. *J. Am. Chem. Soc.* **2003**, *126*, 698–699.

(37) Shen, Y.; Delaglio, F.; Cornilescu, G.; Bax, A. TALOS+: A hybrid method for predicting protein backbone torsion angles from NMR chemical shifts. *J. Biomol. NMR* **2009**, *44*, 213–223.

(38) Fiorin, G.; Klein, M. L.; Hénin, J. Using collective variables to drive molecular dynamics simulations. *Mol. Phys.* **2013**, *111*, 3345–3362.

(39) Vallurupalli, P.; Bouvignies, G.; Kay, L. E. Increasing the Exchange Time-Scale That Can Be Probed by CPMG Relaxation Dispersion NMR. *J. Phys. Chem. B* **2011**, *115*, 14891–14900.

(40) Jaremko, L.; Jaremko, M.; Giller, K.; Becker, S.; Zweckstetter, M. Structure of the mitochondrial translocator protein in complex with a diagnostic ligand. *Science* **2014**, *343*, 1363–6.

(41) Zhou, Y.; Cierpicki, T.; Jimenez, R. H. F.; Lukasik, S. M.; Ellena, J. F.; Cafiso, D. S.; Kadokura, H.; Beckwith, J.; Bushweller, J. H. NMR Solution Structure of the Integral Membrane Enzyme DsbB: Functional Insights into DsbB-Catalyzed Disulfide Bond Formation. *Mol. Cell* **2008**, *31*, 896–908.